Mechanistic study on the corrosion behaviour of Zinc and Zinc-Calcium alloys designed for enhanced metallic coatings in the presence of chloride and phosphate ions

A.D. Malla [a],[*], J.H. Sullivan [a], D.J. Penney [a], T. Dunlop [a], P. Barker [b]

[a] Department of Materials, Faculty of Science and Engineering, Swansea University, Bay Campus, Fabian Way, Crymlyn Burrow, Swansea SA1 8EN, UK
[b] Tata Steel UK Limited, DE Shotton Works, Deeside CH5 2NH, UK

A B S T R A C T

Additions of 1 wt.% Ca were made to Zn (Zn-1Ca) to generate favourable chemical conditions during corrosion for enhanced performance of phosphate inhibitors. Zn-1Ca displayed a reduced corrosion rate in 0.17 M NaCl measured using the Scanning Vibrating Electrode Technique and polarisation. In-situ timelapse microscopy and SEM-EDS demonstrated that intermetallic $CaZn_{13}$ preferentially corroded releasing Ca^{2+} that increased corrosion product precipitation, cathodically deactivating the system. 1×10^{-3} mol dm^{-3} phosphate additions to 0.17 M NaCl decreased the corrosion rate of Zn and Zn-1Ca. Inhibition was greater for Zn-1Ca where uniform precipitation of mixed metal phosphates produced anodic and cathodic inhibition.

1. Introduction

Organically coated galvanised steel is widely used in sectors such as automotive, white goods and construction. The metallic coating layer provides sacrificial protection and is over-coated with an organic layer that acts as a barrier between the metallic coating and the environment. The duplex coating system (organic + metallic layers) provides superior corrosion protection than when metallic or organic coatings are used in isolation [1]. Zinc and its alloys applied via continuous hot-dip galvanising are the dominant metallic coating used on steel. The organic layers consist of pre-treatment, primer, and topcoat. Corrosion inhibitors are usually incorporated into the pre-treatments and the primer layer in the form of pigments that provide further corrosion protection to the system. The inhibitors function by releasing ionic species consequently altering the local electrolytic conditions. These ionic species can produce insulating films either at anodic or cathodic sites by precipitation or by involvement in the electrochemical process [2].

Zinc (Zn) applied via hot-dip galvanising (HDG) to steel corrodes 10–20 times [3] slower than the steel substrate. Further improvements have been achieved through binary (Zinc-Aluminium) (Zn-Al) and ternary (Zinc-Magnesium-Aluminium) (ZMA) alloying additions. The latter has proven to provide improved corrosion resistance over standard Zn and binary Zn-Al due to pH changes induced by the initial attack on $MgZn_2$ rich phases promoting alkaline pH values [4,5] that stabilises zinc phases [6,7] and promote the formation of stable double layered hydroxide corrosion products [8–11]. We have previously shown that further quaternary additions of Germanium (Ge)[12] can enhance the performance further through the preferential release of Mg^{2+} from the microstructure without the concurrent release of hydrolysable Zn^{2+} thus maintaining alkaline pH conditions across the surface of the alloy. These findings provide further opportunities for other elemental additions that may modify the surface electrolyte pH.

Traditionally, HDG systems using Chromium-based hexavalent (Cr (VI)) CrO_4^{2-} or Cr_2O_7 inhibitors have proven to be very effective due to the presence of Cr^{6+} ions. However, these systems have been discontinued due to toxicity and carcinogenicity toward human health and the natural environment [13–16]. Therefore, there is a need for eco-friendly and safe alternative inhibitors. A promising alternative to chromates is phosphate compounds. However, there are some issues due to the inappropriate or extensive use of phosphate such as eutrophication leading to harmful algal blooms, dead zones and death of fish. The phosphate coatings are inexpensive, reasonably hard, highly adherent and electrically non-conductive [17,18]. Typically, in the presence of oxygen, phosphates behave as an anodic inhibitor [1,2,19–21]. However, under certain conditions, such as in presence of divalent metal ions, Ca^{2+}, phosphates may also act as cathodic inhibitors by forming a

surface film that impedes oxygen diffusion to the metal surface [22,23].

In this investigation, we aimed to design a new Zn alloy system through an understanding of its microstructural corrosion mechanisms and subsequent dynamic chemical environment that will provide enhanced performance between the metallic and inhibitor systems. A bulk alloy consisting of 99 wt,% Zn and 1 wt.% Calcium (Zn-1Ca) alloy was produced using Zn ingots obtained from an industrial HDG bath as an initial analogue of a coating to screen successful candidate alloys before upscaling to a coating system. Calcium (Ca) was chosen as it has a more negative standard reduction potential than Zn and thus could be released from the alloy preferentially through Galvanic effects to provide suitable chemical conditions in the electrolyte for increased inhibition efficiency. In Europe commercially available state of art metallic coating system, Zinc magnesium aluminium (ZMA), contains 1–2 wt,% of magnesium and 1–2 wt.% of aluminium hence 1 wt.% of calcium was used as an initial trial in this investigation. Phosphate in the form of Sodium phosphate has been selected as a corrosion inhibitor because of its widespread use in industry. The effects of alloying Zn with Ca in terms of microstructural and electrochemical properties, along with the effects of phosphate addition to the electrochemical properties of Zn and Zn-1Ca were investigated using a range of techniques. Scanning Vibrating Electrode Technique (SVET) was utilised to resolve corrosion features and evaluate relative corrosion performance and Time-lapse Microscopy (TLM) was used to understand the aqueous in-situ corrosion mechanism. The investigation was supported by open-circuit potential, potentiodynamic and linear polarisation resistance measurements.

2. Materials and method

2.1. Materials

The production of Zn and Zn – 1 wt% Ca (Zn-1Ca) samples were completed using a MTI Corporation manufactured KSL-1100X-SV compact crucible melting furnace. Zn ingots which contain 0.2 wt% Al and supersaturated with 0.01 wt% Fe were provided by TATA Steel direct from the HDG bath. Calcium was acquired from Sigma Aldrich and was heated to 600 °C in a crucible before stirring into the HDG melt. After stirring, the melt was further heated to 850 °C and held for 2 min. The melt was then cooled to 600 °C and held for 2 min within the crucible before being splat cast onto a copper plate. The temperature of the melt was measured using the inbuilt temperature controller with ± 1 °C accuracy. Chemicals used; ethanol (C_2H_5OH), sodium hydroxide (NaOH), hydrochloric acid (HCl), nitric acid (HNO_3) and monobasic sodium phosphate (NaH_2PO_4) were supplied by Sigma-Aldrich Chemical Co. and were of analytical grade purity. Aqueous HCl or NaOH was used to adjust the pH of bulk 0.17 mol dm^{-3} NaCl electrolyte.

2.2. Methods

2.2.1. Microstructural analysis

The samples were hot mounted in non-conductive phenolic resin (Metprep Limited), ground to a European P grade P4000 grit using silicon carbide (SiC) paper, polished with aqueous 1 μm diamond slurry, etched using 3 wt% Nital acid and rinsed with distilled water followed by ethanol. Hitachi TM3000 Scanning Electron Microscope (SEM) with a Bruker Energy Dispersive X-ray Spectroscopy (EDS) module was used to obtain images and conduct EDS analysis. The electrical connection was obtained using carbon tape. The area fraction of Zn-1Ca was determined by image analysis of three SEM images. A Bruker D8 Discover X-ray Diffractometer (XRD) with a copper point source (40 kV and 40 mA) was used to identify the phases present within the alloy and the corrosion products. XRD scans were carried out in true parallel beam mode using a goebel mirror, 0.6 mm slit, 1 mm collimator and equatorial soller.

2.2.2. Scanning Vibrating Electrode Technique (SVET)

SVET was utilised to investigate the relative corrosion performance and the localised corrosion characteristics such as the intensity of anodic and cathodic sites. The samples were prepared in the same way as for the microstructural analysis however they were not etched. An area of 36 mm^2 was exposed to the electrolyte, masked using PTFE tape, and 29 measurements were made along both x and y-direction generating 841 data points for each scan. One scan was taken every hour for 24 h and three repeat tests were carried out for each material. All experiments were performed in 0.17 M NaCl at pH 7. The dissolved oxygen concentration within the bulk electrolyte was presumed to be equal to the equilibrium concentration value for air-saturated water i.e., 2.8×10^{-4} mol dm^{-3} [12,24]. SVET has been used comprehensively to understand the surface and cut-edge corrosion of metallic coatings and also the effectiveness of phosphate inhibitors [4,25–29]. A strong relationship has been observed between SVET-derived corrosion inhibition efficiency values calculated using EIS and those obtained from gravimetric mass loss and polarisation data [30].

The SVET measurements were performed using a micro-tip probe with 125 μm diameter platinum wire enclosed in a glass sheath. The probe vibrates perpendicularly at a constant frequency of 140 Hz and an amplitude of 25 μm at 100 μm above the corroding surface. The equipment detail description, operating procedure and calibration procedure can be found in detail elsewhere [12,24,31–33]. During corrosion, potential fields are set up in the electrolyte due to the movement of ionic current flux between anodes and cathodes. As the SVET probe intersects these fluxes an alternating potential is recorded that is proportional to the potential gradient in the direction of vibration that in turn is directly proportional to the ionic current flux thus providing a means of spatially and temporally resolving anodic and cathodic features and their intensity.

2.2.2.1. *Manipulation of SVET data.* SVET is a semi-quantitative metal loss measurement technique as several estimations are made during the calculation process. It is assumed that the corrosion activity remains constant in between the scans and Zn ions (Zn^{2+}) are released during the corrosion process. Metal loss is calculated by the integration of positive current followed by the application of Faraday's law. SVET measured potentials (V) are converted to A m^{-2}, j_z, by multiplying them by the calibration factor and the following integration is performed to get total anodic current (*i*).

$$i = \int_0^x \int_0^y j_z(x,y)dxdy \tag{1}$$

Where x and y are the length and breadth of the scan area. As corrosion activity is assumed to be constant between hourly scans and multiplying the current, *i*, by time, *t*, i.e 3600 s charge, *Q*, is calculated as shown in Eq. (2).

$$Q = i \cdot t \tag{2}$$

Finally, the mass loss is calculated by entering the value of *Q* and the relevant information concerning the corroding material into the Faraday equation as shown in Eq. (3). Total mass loss can be estimated by simply summing the total number of scans.

$$\text{Mass loss(m)} = \frac{Q}{n.F}.Ar \tag{3}$$

Where,
    Q = charge.
    F = Faraday's constant (96,487 C mol^{-1}).
    n = number of electrons (2 for Zn).
    A_r = atomic weight (65 g for Zn).

2.2.2.2. *Limitations of SVET.* SVET assumes a constant corrosion rate in

between scans whereas, in reality, the rate could fluctuate. The SVET measures only the normal component of the current flux and only resolved the anodic and cathodic sites separated by 150 μm [33]. Despite these limitations, the SVET-derived mass losses have been shown to be comparable with those obtained from external Zn runoff tests [29] and an accurate predictor of the relative corrosion performance of Zn coating materials produced under systematically varying conditions [27].

2.2.3. Time-lapse Microscopy (TLM)

Sample surfaces were first prepared in the same way as for the microstructural analysis described in Section 2.2.1. A sample area of 0.785 mm^2 was exposed to electrolyte with the help of 3 M non-conductive polytetrafluoroethylene (PTFE) tape and the sample was securely affixed to the base of the petri dish. A Meiji Techno 7100 optical microscope together with an Infinity 2 digital camera was used to capture images under immersion conditions. The detailed methodology has been described previously [5,12,24]. TLM is a simple and effective technique that enables capturing images of corroding surfaces at a microstructural level under immersion conditions at room temperature. The prepared sample was immersed in 250 ml of 0.17 M NaCl electrolyte at pH 7 and an image was captured every two minutes for up to 24 h. The time-lapse video was compiled using Microsoft Movie Maker with each image having a frame rate of 0.05 s

2.2.4. Electrochemical measurements

Open circuit potential (OCP), potentiodynamic polarisation and linear polarisation resistance (LPR) measurements were performed using a Solartron 1280 potentiostat. Standard calomel electrode (SCE) and platinum-plated electrode were used as a reference and counter electrode respectively. The OCP measurements were conducted for 24 h using a 2-electrode setup. Potentiodynamic and LPR measurements were conducted using a 3-electrode set-up. Potentiodynamic scans were initiated at 150 mV below the OCP scanning in the positive direction for the anodic curve and 150 mV above the OCP scanning in the negative direction for the cathodic curve, both at a rate of 0.166 mV s^{-1}. Anodic and cathodic sweeps were measured independently on fresh samples and the data were merged for analysis. During LPR the samples were polarised by ± 15 mV from open circuit potential (OCP) at a scan rate of 0.166 mV s^{-1}. The samples were finished to European P grade P1200 using SiC paper and rinsed using deionised water and ethanol. An area of 0.78 cm^2 area was exposed to 250 ml of 0.17 M NaCl electrolyte at pH 7. Measurements were initiated in the shortest time possible after the introduction of the electrolyte unless stated. All the electrochemical data presented are the mean values of 2 experiments.

3. Results

3.1. Materials characterisation

The chemical compositions obtained after EDS analysis of the produced samples under investigation are presented in Table 1. The Zn alloy (Zn) was composed of 99.34 ± 0.16 wt.% of Zn, 0.55 ± 0.13 wt.% of Aluminium (Al) and 0.11 ± 0.03 wt.% of Fe. The Zn-1Ca was composed of 98.50 ± 0.26 wt.% of Zn, 0.73 ± 0.15 wt.% of Ca, 0.60 ± 0.17 wt.% of Al and 0.17 ± 0.21 wt.% of Fe.

A microstructural image of Zn and Zn-1Ca captured using optical light microscopy is presented in Fig. 1(a & b). SEM images of Zn and Zn-1Ca alloys captured using a Scanning Electron Microscope (SEM) are

presented in Fig. 1(c & d). Fig. 1(b & d) shows the changes within the microstructure due to the addition of 1 wt% of Ca. The Zn sample has a single-phase microstructure whereas the addition of Ca into the Zn system led to the formation of small, needle-like, dark dendrites as observed in the optical and SEM images shown in Fig. 1(b) & Fig. 1(d).

Energy Dispersive X-Ray Spectroscopy (EDS) was utilised to identify the distribution of elements within the Zn-1Ca alloy. Colour maps identifying the elements Zn and Ca were produced using SEM/EDS software and are presented in Fig. 2b–d. EDS analysis (Fig. 2e) and XRD analysis (Fig. 3) confirm that the new phases formed due to Ca additions were intermetallic CaZn$_{13}$. Previous investigations on the Zn alloys containing Ca have also demonstrated the formation of intermetallic CaZn$_{13}$ [34–36].

The average surface area fraction of CaZn$_{13}$, calculated from 3 different areas of alloy Zn-1Ca, is shown in Table 2. The surface area fraction of the Zn phase was 82.44 ± 1.62 % and 17.56 ± 1.62 % for the CaZn$_{13}$ phase.

3.2. Study of corrosion behaviour of Zn and Zn-1Ca alloys

3.2.1. Investigation of corrosion behaviour using Scanning Vibrating Electrode Technique (SVET)

The SVET was used to investigate the surface corrosion performance of Zn and Zn-1Ca samples over 24 h in an aerated 0.17 M NaCl pH 7 solution. The SVET results include surface normal current density maps, estimated metal loss over 24 h and average hourly estimated metal loss. As Zn was the predominant element in both samples, Zn was selected during the metal loss calculations. Although during the corrosion of Zn-1Ca, both Zn (Zn^{2+}) and Ca (Ca^{2+}) are likely to participate it is difficult to determine the contribution of individual species to metal loss. However, due to the identical charge associated with both ions type the relative metal loss value would be directly comparable across the samples irrespective of the element selected. The SVET-derived metal loss in this investigation was used to compare the relative corrosion performance among samples however the metal loss does not represent an exact metal loss for the experiment period. Besides metal loss, SVET data was used to plot normal current density maps which provide a visual representation of the time-resolved location and intensity of anodic and cathodic activities as recorded by the SVET probe. Red and blue colours are indicative of anodic and cathodic activities respectively.

The SVET-derived metal losses for both Zn and Zn-1Ca after immersion on pH 7 0.17 M NaCl for 24 h are shown in Table 3. The errors shown are based on the standard deviation of three measurements. The derived metal loss for Zn-1Ca was 4.32 ± 1.67 g m^{-2} compared to 9.83 ± 0.75 g m^{-2} for Zn. The alloying of Zn with Ca exhibited a decrease in the measured metal loss by 56 % compared to that of Zn. Therefore, it appears that the addition of Ca has significantly improved the corrosion resistance of Zn-1Ca compared to Zn.

The SVET-derived hourly metal losses (average of three measurements) as a function of time for both Zn and Zn-1Ca during immersion on pH 7 0.17 M NaCl for 24 h are presented in Fig. 4. The errors shown are based on the standard deviation of three measurements. For both samples, the metal loss was ~ 0.10 g m^{-2} for the initial (0 Hr) scan. For Zn, a steep increase in metal loss was then observed from 0 h to 1 h. However, from 1 h onwards up to 20 h, a gradual linear increase with a less steep gradient in metal loss occurred up to a maximum of ~ 0.47 g m^{-2}. Despite the similar metal loss for Zn and Zn-1Ca for the initial scan, in contrast to Zn, the Zn-1Ca hourly metal loss increased with a much lower gradient peaking at a maximum of ~ 0.20 g m^{-2}. This difference in the extent of hourly metal loss suggests that Zn-1Ca had a greater corrosion resistance compared to Zn throughout the 24 h.

Fig. 5 shows the SVET-derived normal current density maps measured above the surface of the Zn and Zn-1Ca samples freely corroding in pH 7 0.17 mol dm^{-3} NaCl for 1 h, 6 h, 12 h, 18 h and 24 h. In both the samples, anodic (red) and cathodic (blue) activities were detected during the initial scans (1-h scans for both Zn and Zn-1Ca).
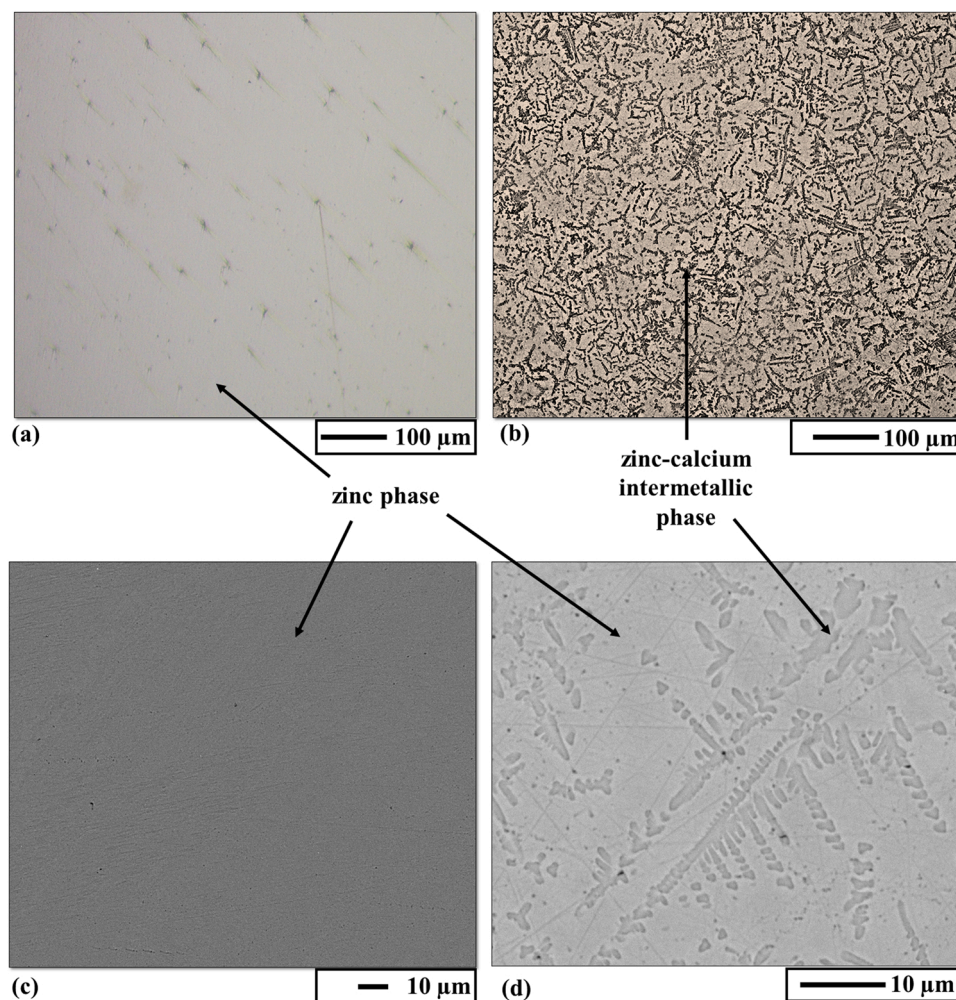
Table 1
Compositions in wt% of the Zn and Zn-Ca alloys.

Sample	Zn (wt.%)	Ca (wt.%)	Al (wt.%)	Fe (wt.%)
Zn	99.34 ± 0.16	/	0.55 ± 0.13	0.11 ± 0.03
Zn-1Ca	98.50 ± 0.26	0.73 ± 0.15	0.60 ± 0.17	0.17 ± 0.21

Fig. 1. Optical microscope images showing the surface of (a) Zn and (b) Zn-1Ca. SEM images showing (c) Zn and (d) Zn-1Ca.

However, a difference in corrosion mechanism was observed between the Zn and Zn-1Ca samples. In the Zn, multiple point anodes were established across the sample surface whereas for Zn-1Ca the exposed surface is approximately diagonally separated into bulk areas of anodic and cathodic activity.

For Zn, the intensity and size of anodes established varied with time. The anodes formed from the onset grew in intensity and radially in size with time. It is also observed that some of the individual anodes passivate with time and new active anodes are formed. In the case of Zn-1Ca, on the contrary, no individual multiple-point anodes are observed during the initial hours. The normal current densities contour maps suggest one-half of the surface exposed is acting as an anode and the other half as a cathode. However, with time a small number of individual point anodes were formed towards the bottom of the scan area and by 24 h of exposure, these were the dominant anodic features on the sample (Fig. 5). It is also observed that the intensity of anodic sites (ii marked on 6-h SVET counter map, Fig. 5) for Zn-1Ca was much lower compared to Zn (i marked on 6-h SVET counter map, Fig. 5). This aligns with Fig. 4 where it was observed the average hourly metal loss for Zn-1Ca was significantly lower compared to Zn. Therefore, these contour maps in Fig. 5 indicate that the corrosion activity occurring on the Zn-1Ca surface was, in general, lower in comparison to the Zn surface throughout the experimental time consequently indicating better corrosion resistance. The change in the morphology of the anodes from point anodes in Zn to a more generalised attack for Zn-1Ca might also indicate a lower rate of through-coating penetration if this alloy were to be used as a metallic coating.

3.2.2. Investigation of corrosion mechanism using Time-lapse Microscopy (TLM)

The improvement in corrosion resistance and the change in the corrosion mechanism of Zn due to 1 wt% of Ca addition were further investigated using TLM. The corrosion mechanism occurring at the microstructural level was observed using TLM. Fig. 6 shows optical microscope images of the Zn surface at various times of immersion in 0.17 M NaCl pH 7. Fig. 6 presents the images captured at 2 min, 2 h, 4 h, 6 h, 8 h and 10 h. Anodic attack, presenting as a dark region, developed from the onset in the upper right quadrant of the exposed sample area, and concurrently darkening of the grain boundaries was also observed (see Video V1). The anode grew in size with respect to time and its growth was seemingly constrained once a grain boundary was reached (see Fig. 6(c–f) and Video V1). As an anode grew in size, corrosion products were precipitated in a form of a semi-circle/ring at a certain distance away from the anode. It has been suggested this ring indicates the boundary between ionic counter currents where the metal ions produced at the anode and hydroxide ions produced at the cathode encounter each other and exceed the solubility product required for precipitation of the corrosion product [19]. The corrosion product ring thickened and was observed to be mobile with time. As the anode grew in size, the corrosion product ring dissolved and re-precipitated away from the anode (see Video V1 and Fig. 6(c) and Fig. 6(f)). This occurrence of re-solubility and precipitation was due to the reduction in local pH at the anodic front. This phenomenon of change in local pH was also observed for ZMA and ZMA-Ge alloys [5,12]. It is also worth noting that the cathodic site (opposite side to the anodic site) where oxygen
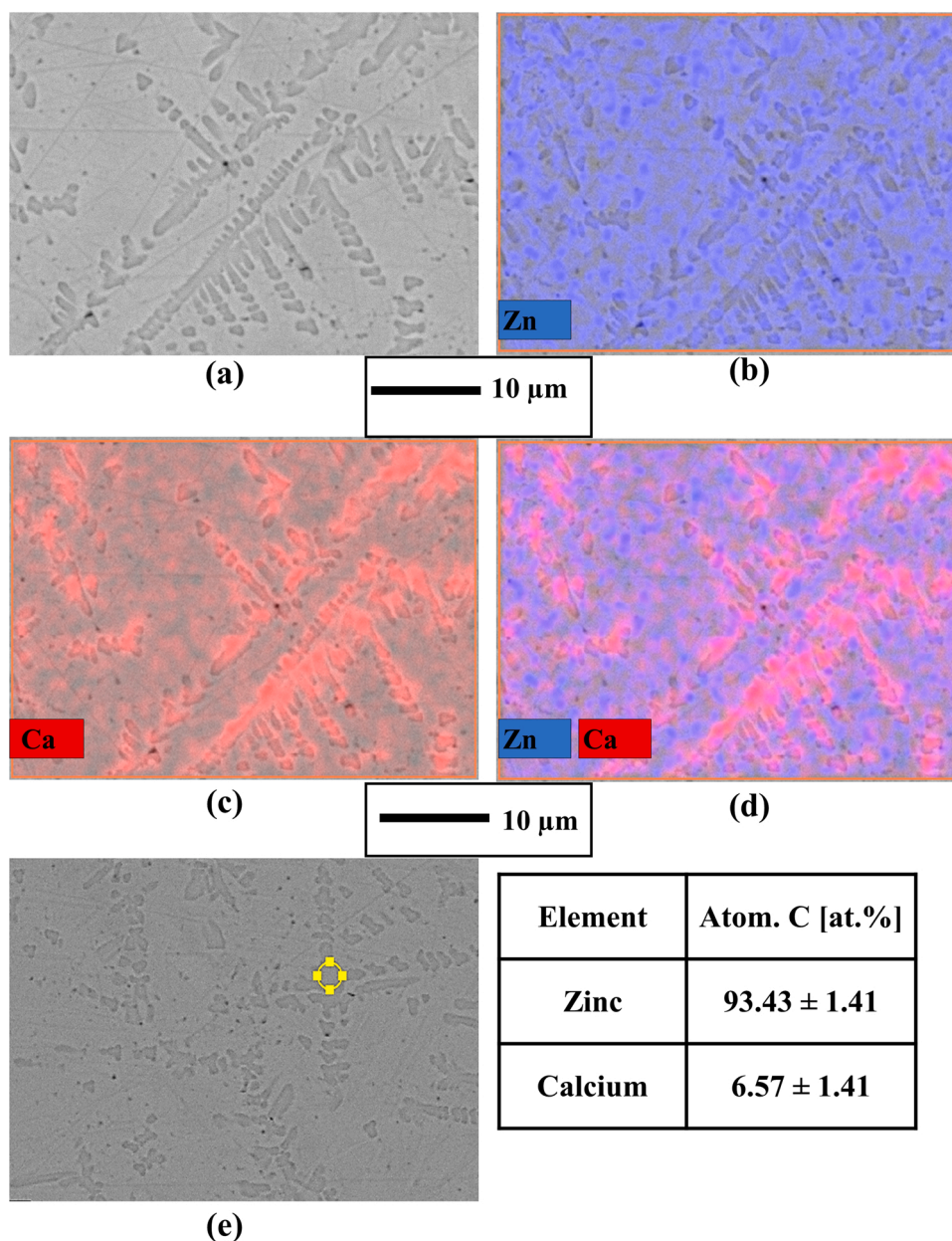
Element	Atom. C [at.%]
Zinc	93.43 ± 1.41
Calcium	6.57 ± 1.41

Fig. 2. (a) SEM image of Zn-1Ca, (b-d) Colour maps for EDS elemental analysis for Zn-1Ca, (e) EDS analysis for Zn-1Ca.

reduction occurs remained clear and no corrosion product precipitation occurred.

Supplementary material related to this article can be found online at doi:10.1016/j.corsci.2022.110956.

Fig. 7 shows optical microscope images of the Zn-1Ca surface at 2 min, 2 h, 4 h, 6 h, 8 h and 10 h of immersion in pH 7 0.17 M NaCl. In contrast to Zn (Fig. 6), multiple anodes were observed at the onset and along with concurrent darkening of the intermetallic metallic phase $CaZn_{13}$ (see Video V2). The 4-minute optical image of Zn-1Ca presented in Fig. 7(a) and video V2 indicates that the anodes appeared to initiate from the intermetallic $CaZn_{13}$ phase. The anodes grew in size with time preferentially via the intermetallic phase $CaZn_{13}$ leaving behind islands of Zn. This preferential attack phenomenon could be observed in video V2 and Fig. 8(b). Similar to Zn, precipitation of corrosion products ring was also observed for Zn-1Ca at a certain distance away from the anodes which grew thicker and denser with time. However, for Zn-1Ca dissolution and re-precipitation of corrosion product ring were not observed instead, the corrosion products continued to precipitate inward, towards

the anode and over the cathodic site (Fig. 7).

Supplementary material related to this article can be found online at doi:10.1016/j.corsci.2022.110956.

3.2.3. Electrochemical measurements

A series of electrochemical experiments; open circuit potential, potentiodynamic polarisation and linear polarisation resistance were performed to further investigate the influence of the addition of 1 wt% Ca into Zn. The experiments commenced immediately after the introduction of the electrolyte. Fig. 9(a) shows the OCP measurements of Zn and Zn-1Ca immersed in pH 7 0.17 M NaCl over 24 h time period. The initial potential was ~ − 1.04 V vs SCE for Zn and ~ − 1.02 V vs SCE for Zn-1Ca after which a shift to more negative potential was observed. The relatively more positive initial potential of Zn-1Ca suggests the oxides films covering the metal surface were much nobler than the oxides films covering the Zn surface. A shift to more negative potential was observed for both Zn and Zn-1Ca. A shift of potential ~ − 0.046 V vs SCE was observed for Zn-1Ca that continued for ~ 2 h whereas, for Zn, the shift

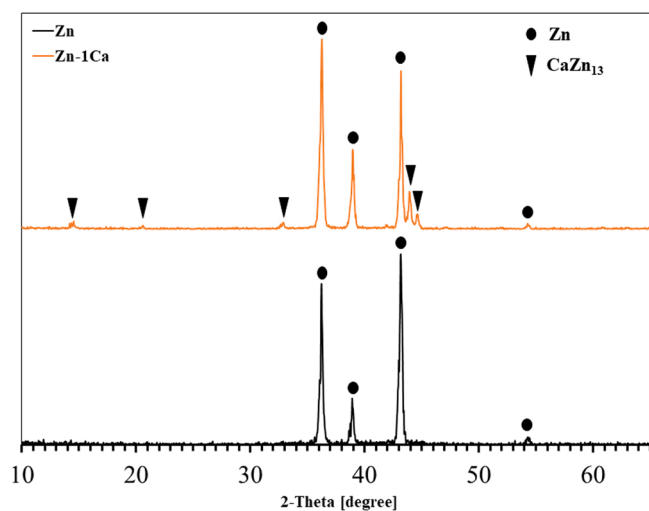**Fig. 3.** XRD analysis of Zn and Zn-1Ca alloys.

Table 2
Area fraction of phases present in Zn-1Ca.

Phase	Area (%)
Zn	82.44 ± 1.62
$CaZn_{13}$	17.56 ± 1.62

Table 3
SVET derived metal loss for Zn and Zn-1Ca after immersion in pH 7 0.17 M NaCl for 24 h.

Sample	Metal loss (g m^{-2})
Zn	9.83 ± 0.75
Zn - 1Ca	4.32 ± 1.67
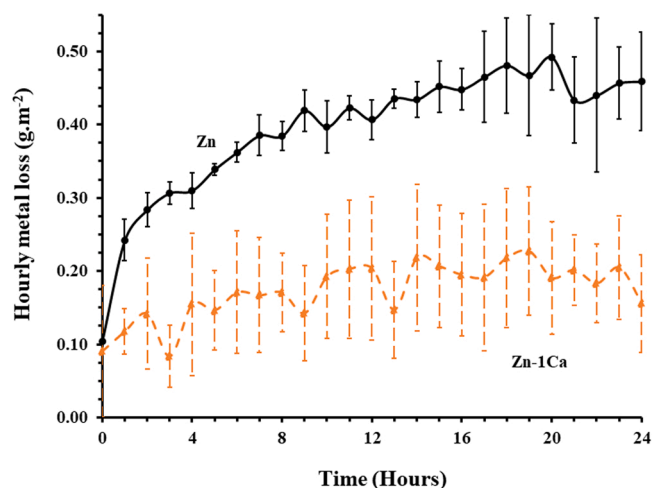
Fig. 4. SVET derived hourly metal loss as a function of time for Zn and Zn-1Ca after immersion in pH 7 0.17 M NaCl solution for 24 h.

was ~ -0.016 V vs SCE lasting ~ 0.5 h.

For Zn, after the initial shift from ~ -1.04 V vs SCE to ~ -1.056 V vs SCE, the potential gradually increased to ~ -1.03 V vs SCE. From ~ -1.03 V vs SCE, the potential again shifts to more negative potential consequently obtaining some degree of stabilisation after ~ 6 h at ~ -1.048 V vs SCE. A similar fluctuation of potential after the initial potential drop was also observed for Zn-1Ca too but at a lower

magnitude. The potential gradually increased from ~ -1.066 V vs SCE to ~ -1.062 V vs SCE. Zn-1Ca stabilised at ~ -1.064 V vs SCE after 4 h, 18 mV lower than that of Zn. This reduction in potential was most likely due to the presence of Ca in the alloy that has a low standard reduction potential of -2.84 V vs SHE compared with -0.76 V vs SHE for Zn. Thus, the mixed potential of the system becomes more negative reflecting the low wt% Ca addition to the material and suggesting that the $CaZn_{13}$ corroded preferentially due to galvanic coupling with the Zn matrix.

Anodic and cathodic potentiodynamic polarisation measurements performed separately on both Zn and Zn-1Ca samples immersed in 0.17 M NaCl pH 7 are presented in Fig. 9(b). The experiments commenced immediately after the introduction of the electrolyte. The polarisation curves demonstrate that there are no obvious changes on the anodic branch due to the addition of 1 wt% of Ca. However, on the cathodic branch, a significant decrease in current was measured for cathodic overpotentials up to 250 mV less than E_{corr}. At -1.20 V vs SCE, the values of the current density (I) showed a large drop (~ 4 times) between the Zn and Zn-1Ca. The current at -1.20 V vs SCE reduced from 2.1×10^{-5} A cm^{-2} for Zn to 8.3×10^{-6} A cm^{-2} for Zn-1Ca.

In order to further understand the relative corrosion rate of Zn and Zn-1Ca, linear polarisation resistance (LPR) measurements were performed. Polarisation resistance (R_p) values measured immediately after the introduction of electrolyte are presented in Table 4. The R_p value of Zn-1Ca was 2.5 times greater than Zn. Therefore, indicating Zn-1Ca provides superior corrosion resistance as i_{corr} α $1/Rp$.

3.2.3.1. Comparison of SVET and LPR measurements. In Fig. 1 the intermetallic $CaZn_{13}$ was spread uniformly (separated by < 100 μm) throughout the Zn-1Ca alloy microstructure and it was observed that the multiple anodes initiated at this intermetallic phase (Fig. 7 and Video V2) before growing into the Zn phase. However, in SVET contour maps (Fig. 5) no focal anodes were established until the 18th hour with a more generalised anodic attack occurring over the surface. As illustrated in Section 2.2.2.2 SVET is only able to resolve individual localised features separated by a distance greater than 150 μm as the SVET scan height is 100 μm. Therefore, for Zn-1Ca the spacing between the cathodic and anodic sites may be less than 150 μm and the lines of current flux between anode and cathode may not intersect the SVET scan plane. However, SVET has resolved the net corrosion activities on the Zn-1Ca surface. By itself, there is a potential the SVET-derived metal loss in Table 3 has been underestimated for Zn-1Ca. However, the linear polarisation resistance measurement suggests that the corrosion kinetics of Zn-1Ca are similarly reduced in comparison to Zn as the R_p value of Zn-1Ca is 2.5 times greater than Zn. This aligns with the SVET measured mass loss reduction of x 2.2 and therefore provides confidence that the corrosion rate of Zn-1Ca is over 2 times lower compared to Zn.

3.2.4. Post-corrosion analysis

In order to understand the contribution of $CaZn_{13}$ to the corrosion resistance afforded by the Zn-1Ca, the corrosion of $CaZn_{13}$ was investigated by completing EDS analysis prior to and following immersion in 0.17 M NaCl pH 7 for 15 min and is presented in Table 5. The errors shown are based on the standard deviation of two measurements. The average weight percentage of Ca calculated using EDS prior to immersion was 4.36 ± 0.32 wt.%. The average weight of Ca in $CaZn_{13}$ intermetallics has dropped to 2.24 ± 0.71 wt.% after 15 min of immersion indicating that the intermetallic phase was being preferentially corroded during the initial exposure to the electrolyte. This preferential corrosion of $CaZn_{13}$ in Zn alloys containing Ca has also been reported previously [37,38]. This preferential attack was likely due to galvanic effects as shown by the reduction in the mixed potential for Zn-1Ca in the OCP measurements due to the presence of calcium in the intermetallic.

Furthermore, the corrosion products formed on the surfaces of Zn and Zn-1Ca after anodic polarisation by $+1.5$ V vs SCE from OCP in pH
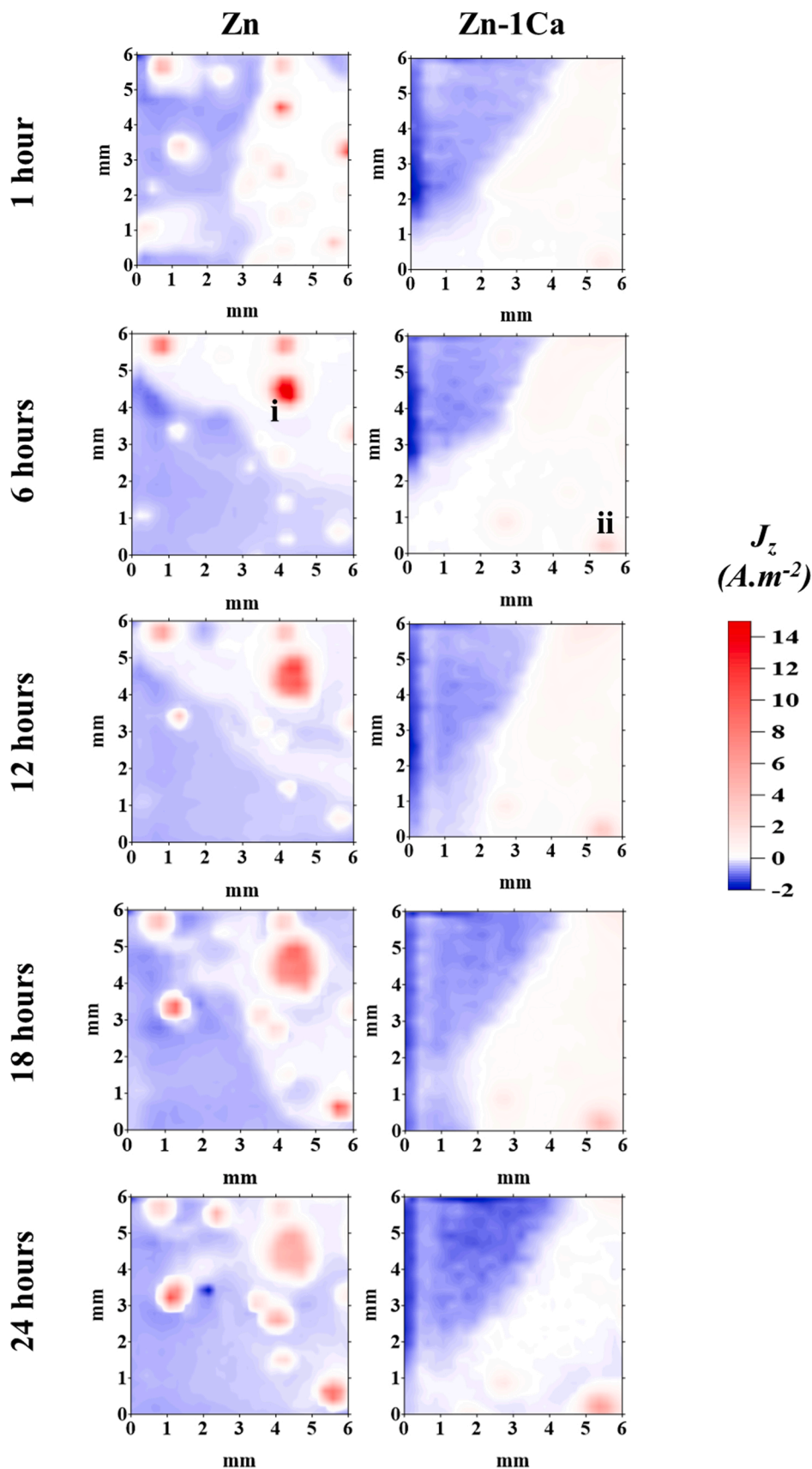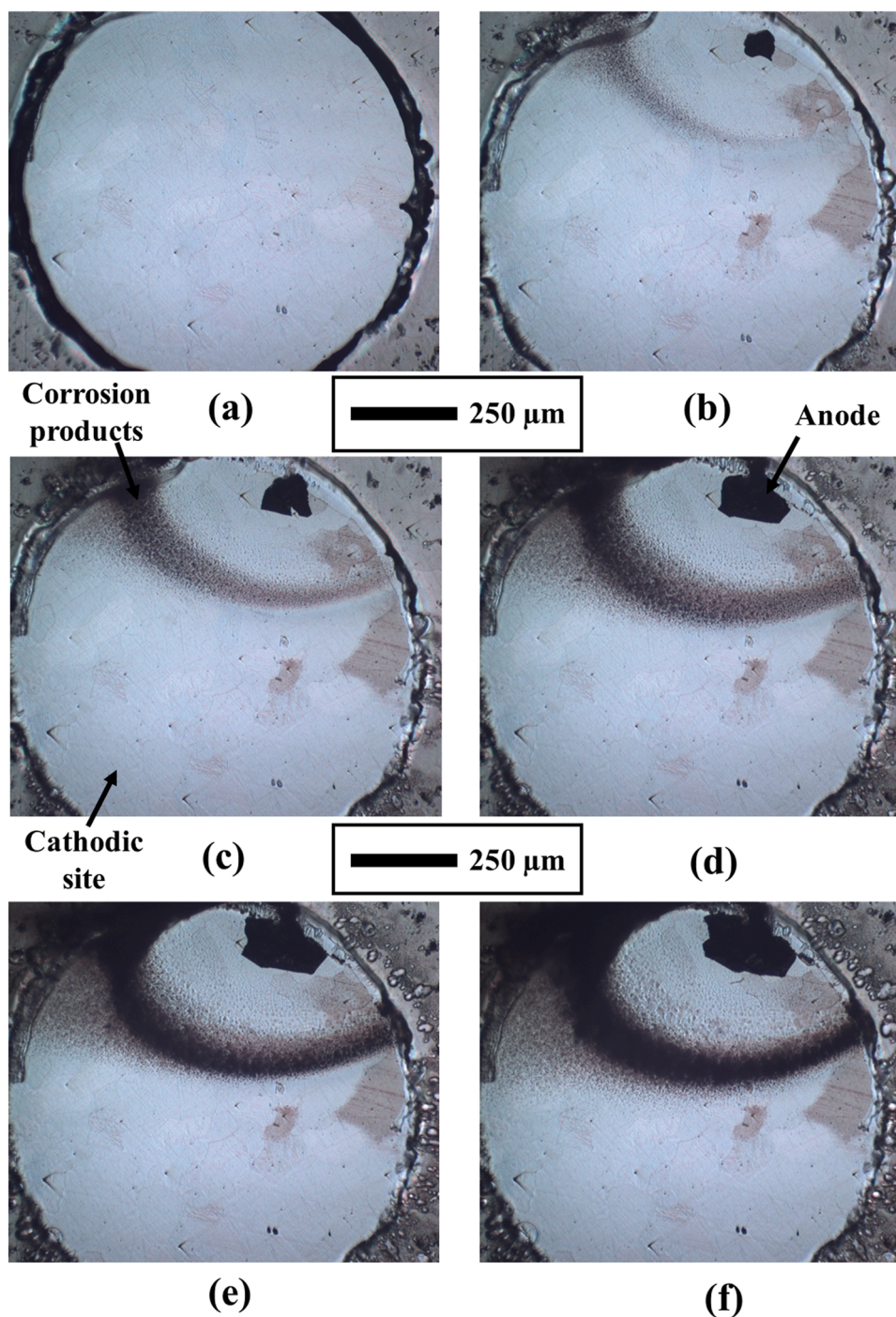
Fig. 5. SVET false colour maps representing normal current density measured above Zn and Zn-1Ca immersed in pH 7 0.17 M NaCl. Anodic activity is displayed as red and cathodic activity as blue.
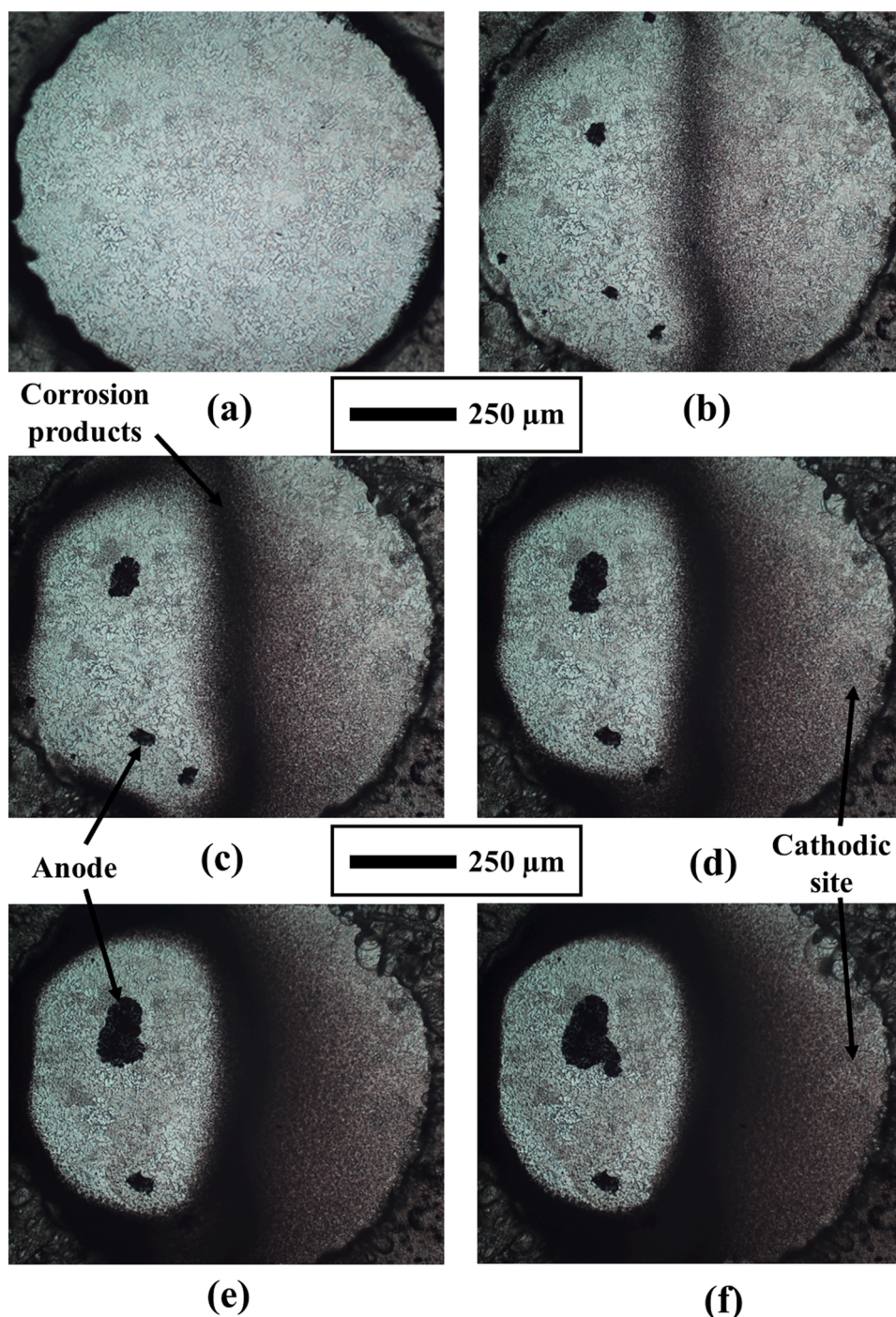
Fig. 6. Time-lapse Microscope images of Zn taken in-situ under immersion conditions in pH 7 0.17 M NaCl. The images (a–f) shown were taken at 2 min, 2 h, 4 h, 6 h, 8 h and 10 h respectively.

7 0.17 M NaCl were analysed using EDS and presented in Table 6. The errors shown are based on the standard deviation of three measurements. For Zn corrosion products, the average weight percentage of Zn and oxygen (O) calculated using EDS was 70.47 ± 8.21 and 29.53 ± 8.21 respectively. Thus, indicative of the formation of $Zn(OH)_2$. Whereas for Zn-1Ca corrosion products, the average weight percentage of Zn, O and Ca calculated using EDS was 86.92 ± 2.21, 10.46 ± 2.77 and 2.62 ± 0.56 respectively. Hence for Zn-1Ca, EDS analysis suggested the formation of a small quantity of Ca corrosion products in addition to Zn corrosion products.

3.3. Study of the inhibition effects of phosphate during corrosion of Zn and Zn-1Ca alloys

A further investigation was conducted to evaluate the performance of phosphate ions on the inhibition of corrosion of Zn and Zn-1Ca. Sodium phosphate (Na_3PO_4) was used as a source of phosphate ions. The 0.17 M NaCl was dosed with 1×10^{-3} mol dm^{-3} sodium phosphate and was adjusted to pH 7. The inhibitor concentration of 1×10^{-3} mol dm^{-3} was selected because of its proven inhibition efficiency previously of 92 % on ZMA coatings [24].

Fig. 7. Time-lapse Microscope images of Zn-1Ca taken in-situ under immersion conditions in pH 7 0.17 M NaCl. The images (a-f) shown were taken at 2 min, 2 h, 4 h, 6 h, 8 h and 10 h respectively.

3.3.1. Investigation of inhibition effect of Phosphate using Scanning Vibrating Electrode Technique (SVET)

The SVET was utilised to investigate the effect of sodium phosphate (Na_3PO_4) as an inhibitor on Zn and Zn-1Ca. The SVET-derived metal loss for both Zn and Zn-1Ca after immersion on pH 7 0.17 M NaCl containing 1×10^{-3} mol dm^{-3} Na_3PO_4 for 24 h and 48 h are shown in Table 7. The errors shown are based on the standard deviation of three measurements. The derived metal loss for Zn-1Ca was 1.19 g m^{-2} compared to 5.12 g m^{-2} for Zn for 24 h. The addition of sodium phosphate had a significant impact on SVET-derived metal loss. For both Zn and Zn-1Ca, a reduction in metal loss of 48 % and 72 % was observed respectively

(Table 3 and Table 7). Although the metal loss for both Zn and Zn-1Ca had significantly decreased with the addition of sodium phosphate, the effectiveness to inhibit corrosion was much higher in Zn-1Ca compared to Zn. Zn-1Ca alloy in pH 7 0.17 M NaCl containing 1×10^{-3} mol dm^3 sodium phosphate provided a 91 % reduction in metal loss compared to Zn in pH 7 0.17 M NaCl. The metal loss of Zn and Zn-1Ca with/without Na_3PO_4 was in the order Zn (9.83 g m^{-2}) > Zn + Na_3PO_4 (5.12 g m^{-2}) > Zn-1Ca (4.32 g m^{-2}) > Zn-1Ca + Na_3PO_4 (1.19 g m^{-2}) (Table 3 and Table 7). Therefore, it is reasonable to assume that the significant enhancement of the effectiveness of Na_3PO_4 in Zn-1Ca could be due to the presence of Ca.
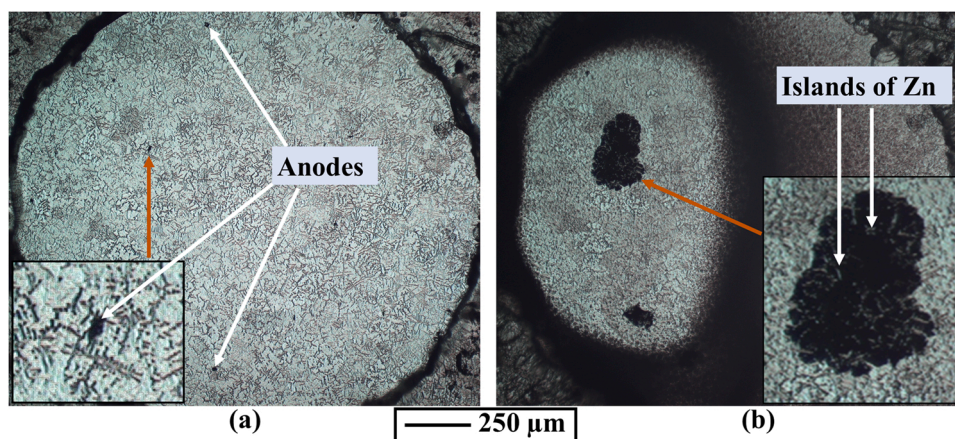
Fig. 8. Time-lapse Microscope images of Zn-1Ca taken in-situ after (a) 4 min and (b) 8 h under immersion conditions in pH 7 0.17 M NaCl.
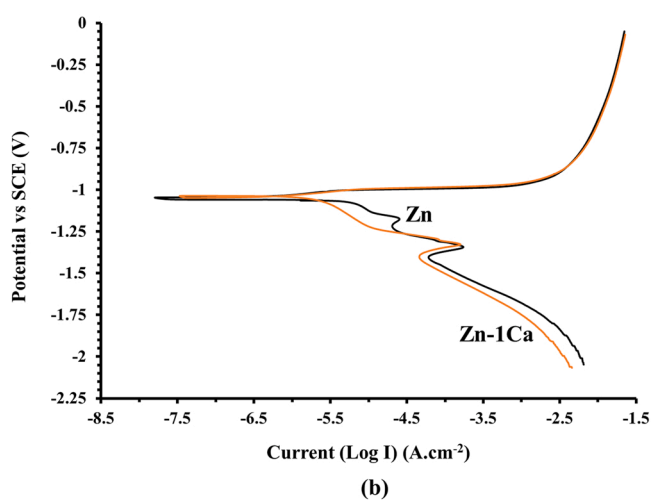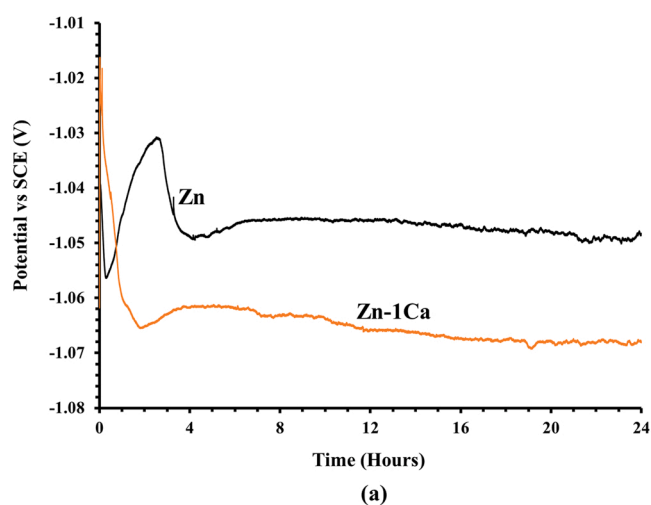

(a)

(b)

Fig. 9. (a) The time-dependent OCP for Zn and Zn-1Ca immersed in pH 7 0.17 M NaCl for 24 h (b) Polarisation curves for Zn and Zn-1Ca immersed in pH 7 0.17 M NaCl solution.

Table 4

Linear polarisation resistance measurements obtained for Zn and Zn-1Ca where the samples were polarised by ± 15 mV at a scan rate of 0.166 mV s^{-1} in pH 7 0.17 M NaCl.

Sample	Polarisation resistance, R_p, (Ohms cm^{-2})
Zn	4438.6
Zn - 1Ca	12,141.0

Table 5

EDS analysis of intermetallics CaZn$_{13}$ prior to and after 15 min of immersion in 0.17 M NaCl pH 7 solution.

Element	Prior immersion	After immersion
Zinc (wt.%)	95.65 ± 0.32	97.30 ± 0.92
Calcium (wt.%)	4.36 ± 0.32	2.24 ± 0.71

Table 6

EDS analysis of corrosion products formed on the surfaces of Zn and Zn-1Ca after anodic polarisation by $+ 1.5$ V vs SCE from OCP in pH 7 0.17 M NaCl.

Element	Zn	Zn-1Ca
Zn (wt.%)	70.47 ± 8.21	86.92 ± 2.21
Oxygen (wt.%)	29.53 ± 8.21	10.46 ± 2.77
Calcium (wt.%)	/	2.62 ± 0.56

Table 7

SVET-derived metal loss for Zn and Zn-1Ca after immersion in pH 7 0.17 M NaCl containing 1×10^{-3} mol dm^3 sodium phosphate for 24 h and 48 h.

Sample	Metal loss for 24 h (g m^{-2})	Metal loss for 48 h (g m^{-2})
Zn	5.12 ± 1.27	14.57 ± 1.74
Zn-1Ca	1.19 ± 0.42	7.01 ± 2.84

metal loss from the 25th h to the 48th h with Na$_3$PO$_4$ additions as compared to the metal loss for 1–24 h without Na$_3$PO$_4$ additions for Zn and Zn-1Ca is presented in Table 8. These data suggest that the Na$_3$PO$_4$

Table 8

SVET-derived metal loss for Zn and Zn-1Ca after immersion in pH 7 0.17 M NaCl with and without 1×10^{-3} mol dm^{-3} sodium phosphate addition.

Sample	Metal loss from 25th h to 48th h with phosphate (g m^{-2})	Metal loss for 24 h without phosphate (g m^{-2})
Zn	9.45 ± 1.94	9.83 ± 0.75
Zn-1Ca	5.82 ± 3.21	4.32 ± 1.67

Further experiments were performed using SVET for 48 h to assess if the inhibition effect persisted. After 48 h with Na$_3$PO$_4$ additions, the SVET-derived metal loss for Zn-1Ca was reduced by 51 % to 7.01 g m^{-2} compared to 14.57 g m^{-2} for Zn. Therefore, Zn-1Ca was providing twice the resistance compared to Zn. After the 48-h SVET experiments, the

had a reduced inhibition effect after 24 h as the metal loss values were similar to those recorded over 24 h when no phosphate was added.

To further explore the time-resolved mass loss kinetics from SVET, the SVET derived hourly metal loss (average of three measurements) as a function of time for both Zn and Zn-1Ca during immersion on pH 7 0.17 M NaCl containing 1×10^{-3} mol dm^{-3} Na$_3$PO$_4$ for 24 h and 48 h are presented in Fig. 10 and Fig. 11 respectively. The addition of 1×10^{-3} mol dm^{-3} Na$_3$PO$_4$ significantly reduced the rate of hourly metal loss from the onset for both Zn and Zn-1Ca and Fig. 10 shows that Na$_3$PO$_4$ was much more effective in presence of Ca. Considering these data for both Zn and Zn-1Ca with Na$_3$PO$_4$, the hourly mass loss values began to increase towards those of the uninhibited systems after 24 h. With further time the effect of Ca and Na$_3$PO$_4$ reduced as the hourly metal loss plots for Zn + Na$_3$PO$_4$ and Zn-1Ca + Na$_3$PO$_4$ started to converge after 42 h as shown in Fig. 11.

Fig. 12 shows the normal current densities measured above the surface of the Zn freely corroding in pH 7 0.17 mol dm^{-3} NaCl containing 1×10^{-3} mol dm^{-3} Na$_3$PO$_4$ for 1 h, 6 h, 12 h, 18 h and 24 h. The addition of Na$_3$PO$_4$ led to the passivation of the exposed surface for a short period as no anodic or cathodic features were present for the 1st h. However, from 6 h onwards multiple-point anodes were established. The addition of Na$_3$PO$_4$ also significantly reduced the number and intensity of the established anodic features. The SVET contour maps for 12 h, 18 h and 24 h indicate that the established anodes did not grow radially as was observed for Zn without Na$_3$PO$_4$ (Fig. 5) but new anodic features developed around the already established anodic site.

Fig. 13 shows the normal current densities measured above the surface of the Zn-1Ca freely corroding in pH 7 0.17 mol dm^{-3} NaCl containing 1×10^{-3} mol dm^{-3} Na$_3$PO$_4$ for 1 h, 6 h, 12 h, 18 h and 24 h. The presence of Ca and Na$_3$PO$_4$ had a significant impact on the measured current densities and led to an extended period of passivation of the exposed surface as no anodic or cathodic features were present for up to 12 h. The anodic features were established within 18 h and grew in intensity and size with time. The mechanism observed for Zn-1Ca, i.e. $\sim$ half the exposed surface behaving as an anodic site and the other half as a cathodic site, was not observed with Na$_3$PO$_4$ additions as focal anodes are present on 18 h and 24 h scans.

3.3.2. Investigation of inhibition effect of phosphate using Time-lapse Microscopy (TLM)

To assess the behaviour and role of Na$_3$PO$_4$ on the enhancement of corrosion resistance observed during SVET experiments further investigation was conducted utilising TLM. Fig. 14 shows optical microscope images of the surfaces of Zn after various times of immersion in pH 7 0.17 mol dm^{-3} NaCl containing 1×10^{-3} mol dm^{-3} Na$_3$PO$_4$. Fig. 14 features the images captured at 2 min, 2 h, 6 h, 12 h, 18 h and 24 h. It can be observed that two anodes developed from the onset, concurrently
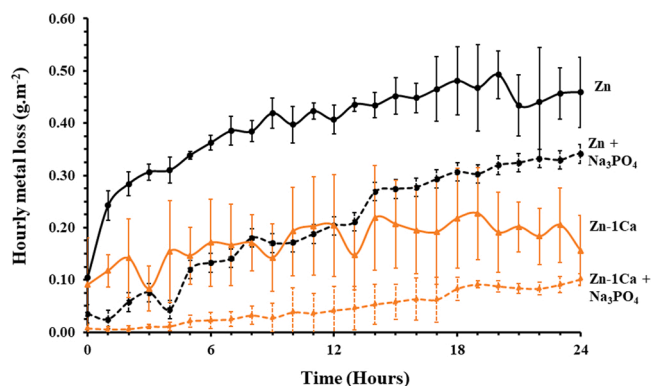

Fig. 10. SVET derived hourly metal loss as a function of time for Zn and Zn-1Ca after immersion in pH 7 0.17 M NaCl with and without 1×10^{-3} mol dm^{-3} Na$_3$PO$_4$ addition for 24 h.
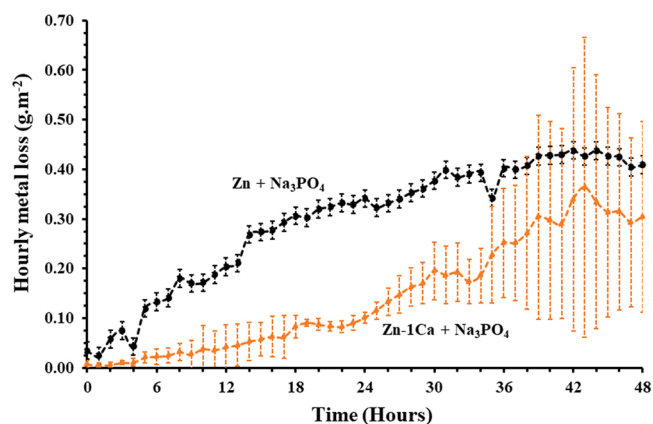

Fig. 11. SVET derived hourly metal loss as a function of time for Zn and Zn-1Ca after immersion in pH 7 0.17 M NaCl containing 1×10^{-3} mol dm^{-3} Na$_3$PO$_4$ for 48 h.

darkening the grain boundaries similar to Zn without Na$_3$PO$_4$ (see Video V1). The addition of Na$_3$PO$_4$ has drastically altered the corrosion products precipitation phenomenon. For Zn, precipitation of corrosion products occurred at a certain distance away from the anode (Fig. 6 and Video V1) however in the presence of phosphate ions corrosion products were precipitated on top or in the vicinity of the anode (Fig. 14 and Video V3). It is also observed that the precipitation of these corrosion products restricted the growth of the anodes. However, with time the initiated anodes grew in diameter and eventually led to the formation of a corrosion product. Throughout the experiment, the cathodic region remained free from corrosion product precipitation (left-hand side of images in Fig. 14).

Supplementary material related to this article can be found online at doi:10.1016/j.corsci.2022.110956.

Fig. 15 shows optical microscope images of the surface of Zn-1Ca at 2 min, 2 h, 6 h, 12 h, 18 h and 24 h of immersion in pH 7 0.17 M NaCl containing 1×10^{-3} mol dm^{-3} Na$_3$PO$_4$. The presence of phosphate ions drastically altered the corrosion behaviour of the Zn-1Ca (Video V4 and Fig. 15). Contrary to Zn where the formation of anodes at the Zn phase was observed at the onset, no such activity was observed for Zn-1Ca. However, with time darkening of the intermetallic CaZn$_{13}$ was observed. The darkening of intermetallic started from the periphery of the exposed area and then proceeded inwards. As the darkening of the intermetallic continued it led to the formation of a precipitate that generally covered the exposed surface with some small patches of uncovered areas. For the experimental time of 24 h, the bulk Zn phase was protected from anodic attack as no focal anodes as seen for Zn samples were observed for Zn-1Ca.

Supplementary material related to this article can be found online at doi:10.1016/j.corsci.2022.110956.

3.3.3. Electrochemical measurements

Open circuit potential measurements were performed to assess the behaviour of Zn and Zn-1Ca in pH 7 0.17 M NaCl containing 1×10^{-3} mol dm^{-3} Na$_3$PO$_4$. The results obtained are presented in Fig. 16. In the presence of phosphate ions, there was a steep increase in potential from the onset for both Zn and Zn-1Ca. The gradient of the potential increment was higher in Zn-1Ca compared to Zn. Zn-1Ca took $\sim$ 1.5 h to reach its maximum potential of ~ -1.01 V vs SCE whereas Zn took $\sim$ 3.5 h to reach its maximum potential of ~ -1.02 V vs SCE.

From the highest positive potential for both samples, there was a similar shift towards more negative potentials with both materials obtaining some degree of stabilisation at $\sim$ 1.05 V vs SCE for Zn and $\sim$ 1.04 V vs SCE for Zn-1Ca. However, Zn took $\sim$ 8 h from the onset of the experiment to obtain this stabilisation compared to Zn-1Ca taking 12 h. Also, in contrast to Zn, Zn-1Ca obtained some degree of
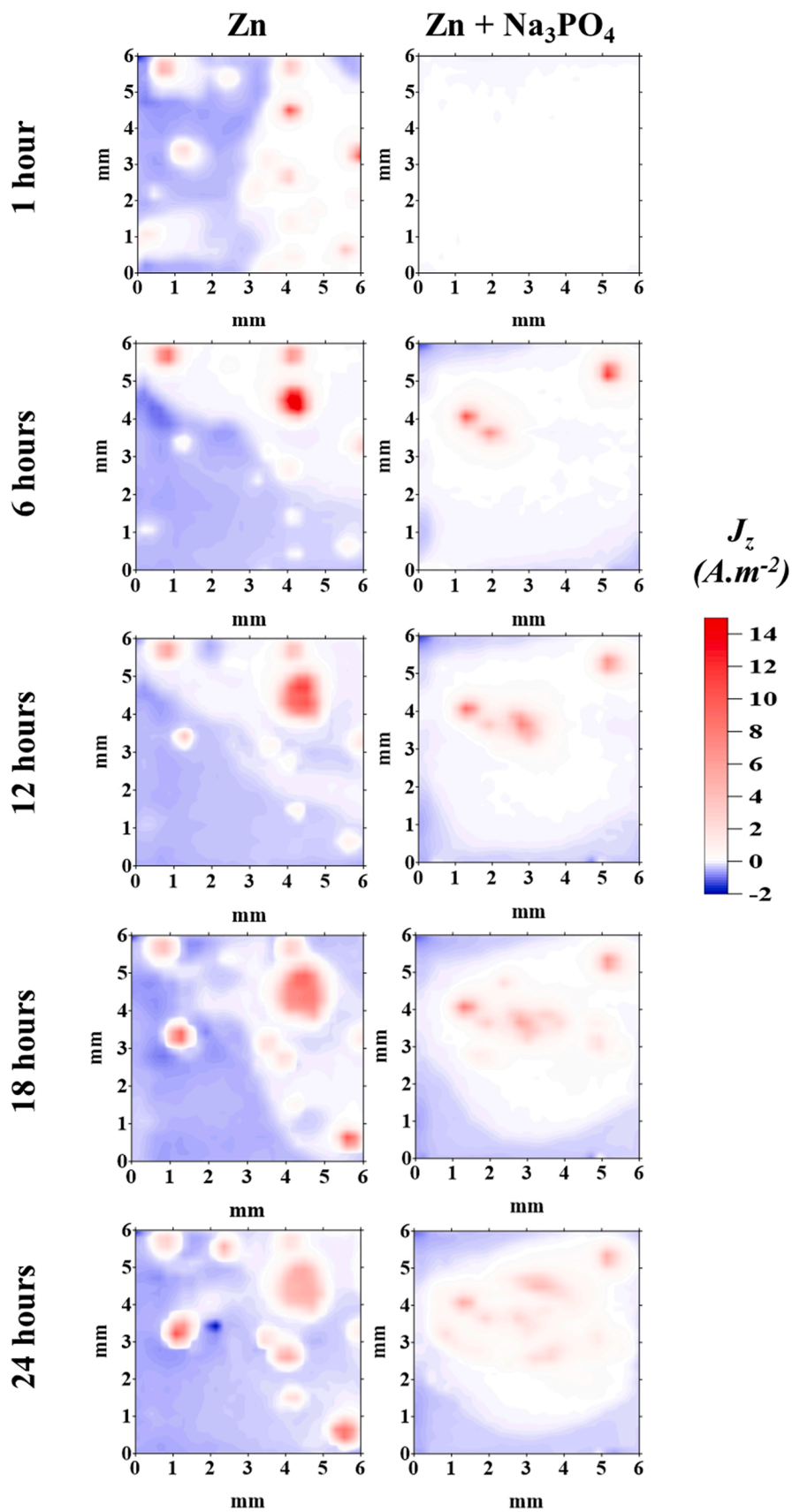
Fig. 12. SVET false colour maps representing normal current density measured above Zn immersed in pH 7 0.17 M NaCl containing 1×10^{-3} mol dm^{-3} Na$_3$PO$_4$.
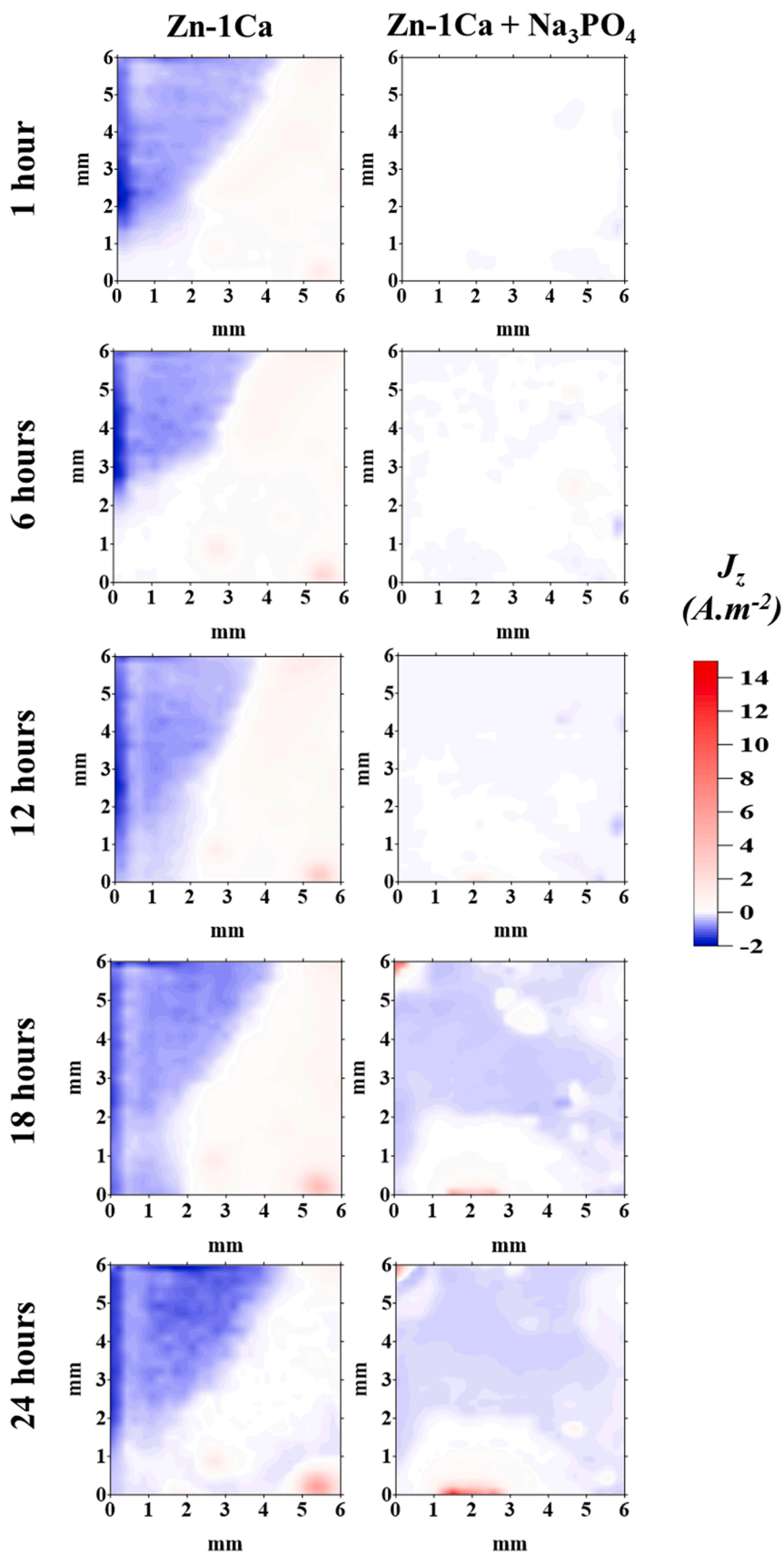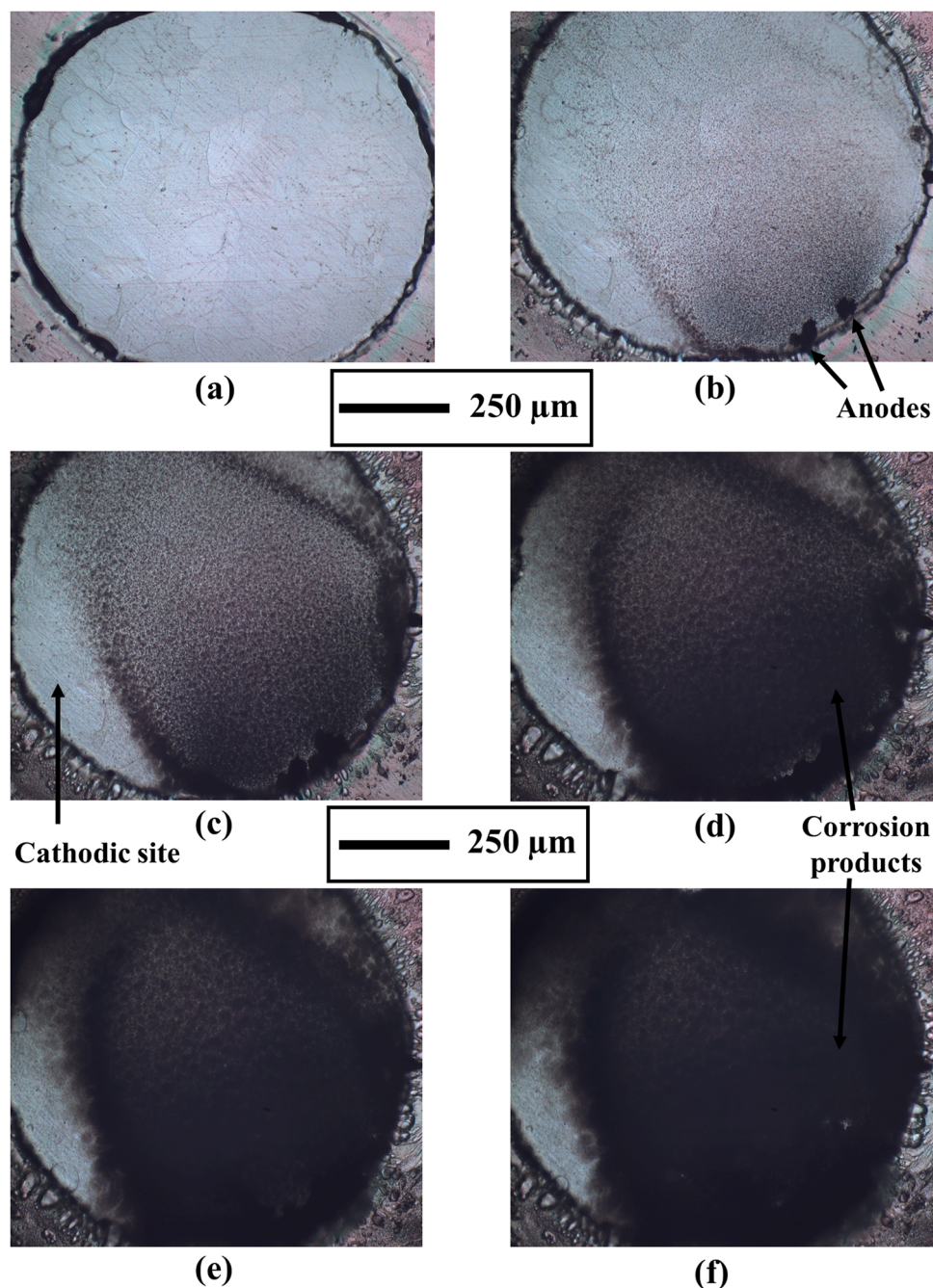
Fig. 13. SVET false colour maps representing normal current density measured above Zn-1Ca immersed in pH 7 0.17 M NaCl containing 1×10^{-3} mol dm^{-3} Na$_3$PO$_4$.
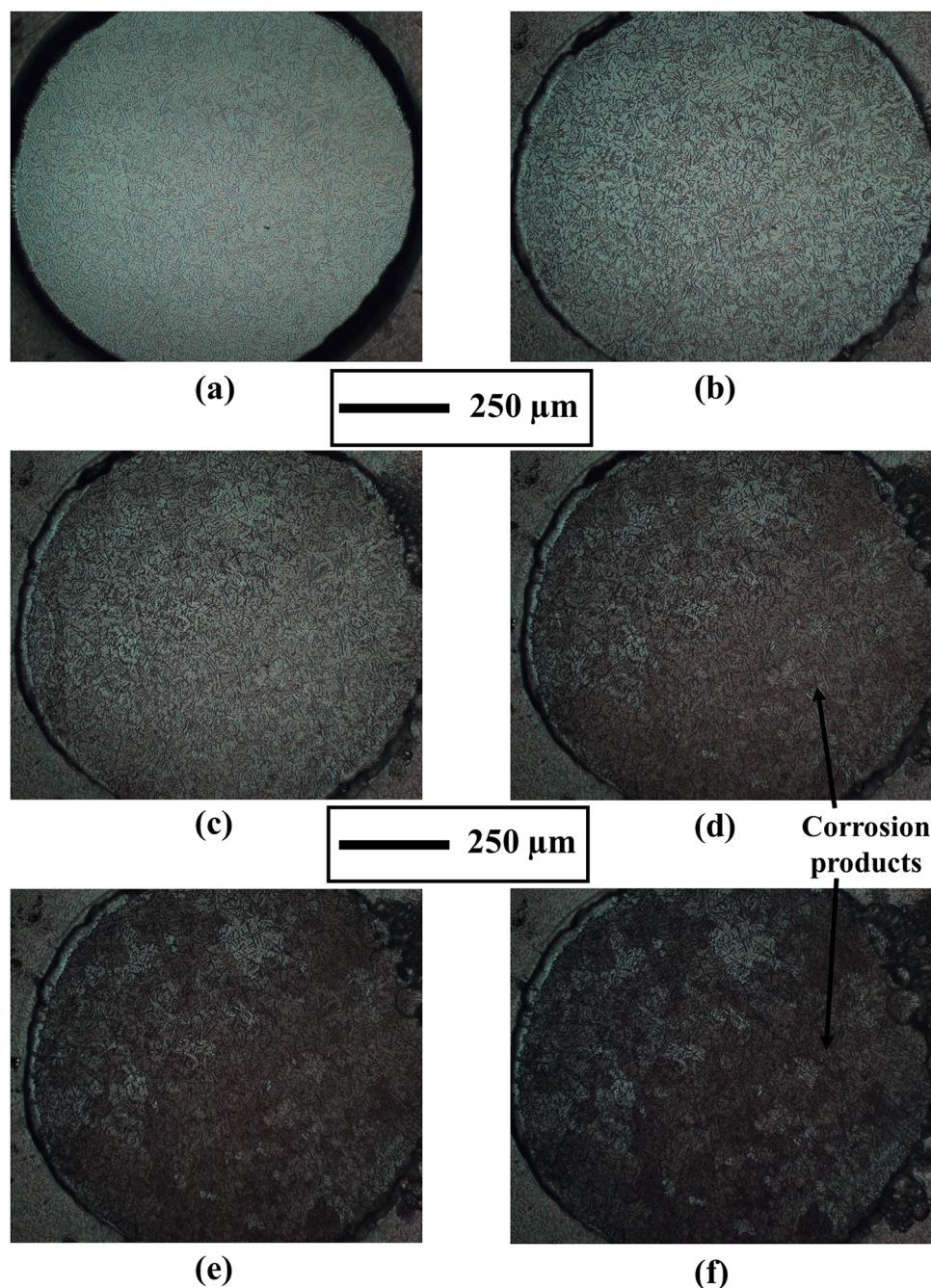
Fig. 14. Time-lapse Microscope images of Zn taken in-situ under immersion conditions in pH 7 0.17 M NaCl containing 1×10^{-3} mol dm^{-3} Na$_3$PO$_4$. The images (a-f) shown were taken at 2 min, 2 h, 6 h, 12 h, 18 h and 24 h respectively.

stabilisation at ~ 1.026 V vs SCE after 4 h before final stabilisation at ~ 1.045 V vs SCE after 12 h.

The mechanism of corrosion product deposition observed in Fig. 14, the rise in OCP for both alloys in comparison with their respective controls, along with the literature [19,39] indicates that phosphate may act as an anodic inhibitor. Therefore, further anodic and cathodic polarisation experiments were performed to gain more insight into this behaviour. The samples were allowed to corrode freely for 135 min to gain a stable OCP in the electrolyte (with and without phosphate additions) before conducting polarisation experiments. This procedure was adopted because the OCP measurements (Fig. 16) for Zn and Zn-1Ca in the phosphate-containing electrolyte indicated that after approximately 2 h, Zn and Zn-1Ca obtained their most positive potentials, hence suggesting maximum phosphate deposition after this time.

In Fig. 17 (a), the anodic polarisation curves demonstrated that in the absence of phosphate ions, the addition of 1 wt% Ca to Zn shifted the E_{corr} by 20 mV to a more negative potential. The curves for Zn and Zn-1Ca appeared somewhat similar with regards to their initial Tafel slopes but Zn-1Ca showed a very small change in current observed between -1.030 V vs SCE to -0.990 V vs SCE. In presence of 1×10^{-3} mol dm^{-3} Na$_3$PO$_4$, E_{corr} of Zn shifted to more positive potential (anodic) by 10 mV. Similarly for Zn-1Ca in presence of 1×10^{-3} mol dm^{-3} Na$_3$PO$_4$ E_{corr} shifted to a more positive potential by 20 mV. In presence of phosphate ions, the anodic current was inhibited significantly for both Zn and Zn-1Ca with a greater reduction in anodic current observed for the Zn-1Ca sample. For example, at -0.99 V vs SCE the anodic current was $\sim - \text{Log } 5.72$ (A cm^{-2}) for Zn-1Ca and $\sim - \text{Log } 5.05$ (A cm^{-2}) for Zn when phosphate was present compared to $\sim - \text{Log } 3.50$ (A cm^{-2}) for

Fig. 15. Time-lapse Microscope images of Zn-1Ca taken in-situ under immersion conditions in pH 7 0.17 M NaCl containing 1×10^{-3} mol dm^{-3} Na$_3$PO$_4$. The images (a–f) shown were taken at 2 min, 2 h, 6 h, 12 h, 18 h and 24 h respectively.

both Zn and Zn-1Ca without phosphate ions. A more significant passive region was observed for the Zn-1Ca sample in the presence of phosphate compared with the Zn sample.

In Fig. 17 (b), the cathodic polarisation curves of both Zn and Zn-1Ca demonstrated cathodic inhibition in presence of phosphate, especially at potentials within − 100 mV of E$_{corr}$. However, the inhibition was much greater and persisted over a greater range of cathodic potentials in presence of Calcium. Although cathodic inhibition is demonstrated for both Zn and Zn-1Ca in the presence of phosphate, the predominant mechanism appears to be anodic inhibition due to the shift of E$_{corr}$ to more positive potentials.

LPR measurements were also performed after OCP stabilisation for 135 min. Polarisation resistance (R$_p$) values are presented in Table 9. The R$_p$ value of Zn-1Ca was greater than Zn. Therefore, indicating Zn-

1Ca provided better corrosion resistance as $i_{corr} \propto 1/R_p$.

3.3.4. Post-corrosion analysis

The corrosion products formed on the surfaces of Zn and Zn-1Ca after anodic polarisation in pH 7 0.17 M NaCl containing 1×10^{-3} mol dm^{-3} sodium phosphate were analysed using EDS. The EDS results obtained are presented in Table 10. The errors shown in Table 10 are based on the standard deviation of three measurements. For Zn corrosion products, the average weight percentage of Zn, O and Phosphorus (P) calculated using EDS was 62.2 ± 5.16, 28.05 ± 3.74 and 9.76 ± 1.50 respectively. Hence, indicating the formation of corrosion products containing zinc, oxygen and phosphorus.

For Zn-1Ca corrosion products, the average weight percentage of Zn, O, P and Ca calculated using EDS was 67.64 ± 24.62, 22.81 ± 16.40,
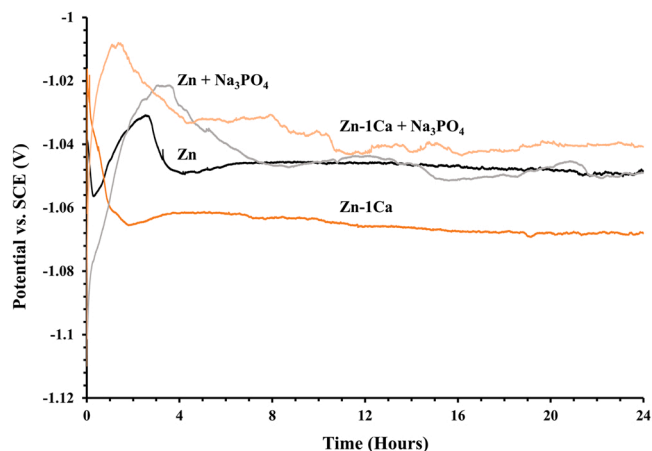
Fig. 16. The time-dependent OCP for (a) Zn and (b) Zn-1Ca (c) Zn + Na$_3$PO$_4$ (d) Zn-1Ca + Na$_3$PO$_4$ immersed in pH 7 0.17 M NaCl for 24 h.
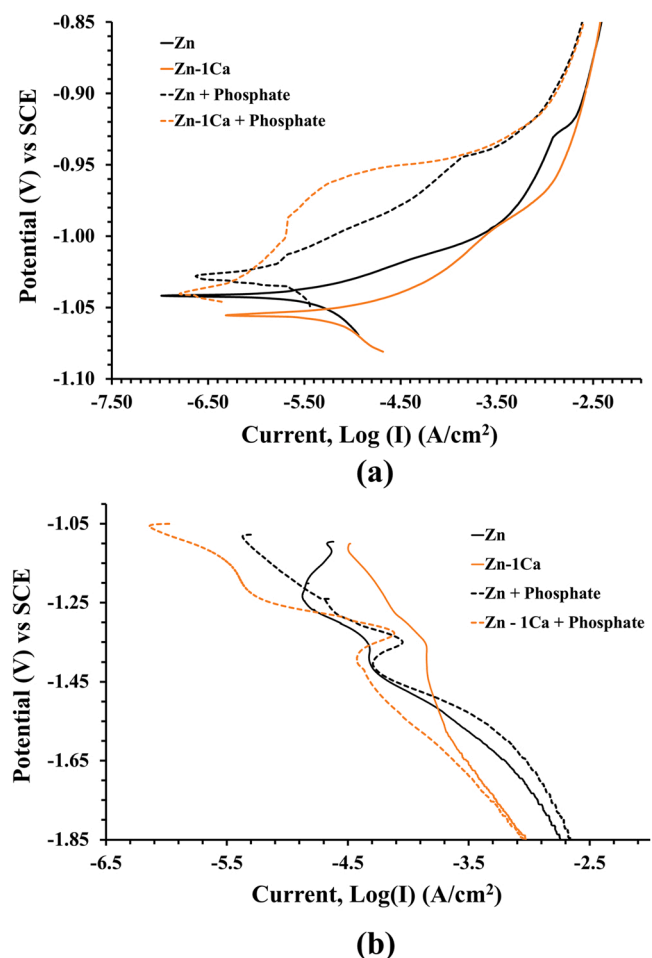

(a)

(b)

Fig. 17. Plot of (a) anodic and (b) cathodic polarisation curves for Zn, Zn-1Ca, Zn + Na$_3$PO$_4$ and Zn-1Ca + Na$_3$PO$_4$ immersed in pH 7 0.17 M NaCl after OCP stabilisation for 135 min.

8.37 ± 8.71 and 1.18 ± 1.50 respectively. The analysis indicated the corrosion products formed contain Zn, Ca, O and phosphorus.

The XRD spectra of corrosion products formed on the Zn and Zn-1Ca surfaces after anodic polarisation in pH 7 0.17 M NaCl containing 1×10^{-3} mol dm^{-3} sodium phosphate are presented in Fig. 18. It can be seen that zinc phosphate is present in both Zn and Zn-1Ca. However, the

Table 9

Linear polarisation resistance measurements obtained for Zn and Zn-1Ca where the samples were polarised by ± 15 mV at a scan rate of 0.166 mV s^{-1} in pH 7 0.17 M NaCl after OCP stabilisation for 135 min.

Sample	Polarisation resistance, Rp, (Ohms cm^{-2})
Zn + Na$_3$PO$_4$	13,494.00
Zn-1Ca + Na$_3$PO$_4$	15,134.00

Table 10

EDS analysis of corrosion products formed on the surfaces of Zn and Zn-1Ca after anodic polarisation by + 1.5 V vs SCE from OCP from pH 7 0.17 M NaCl containing 1×10^{-3} mol dm^{-3} sodium phosphate.

Elements	Zn	Zn-1Ca
Zn (wt.%)	62.2 ± 5.16	67.64 ± 24.62
Oxygen (wt.%)	28.05 ± 3.74	22.81 ± 16.40
Phosphorus (wt.%)	9.76 ± 1.50	8.37 ± 8.71
Calcium (wt.%)	/	1.18 ± 1.50

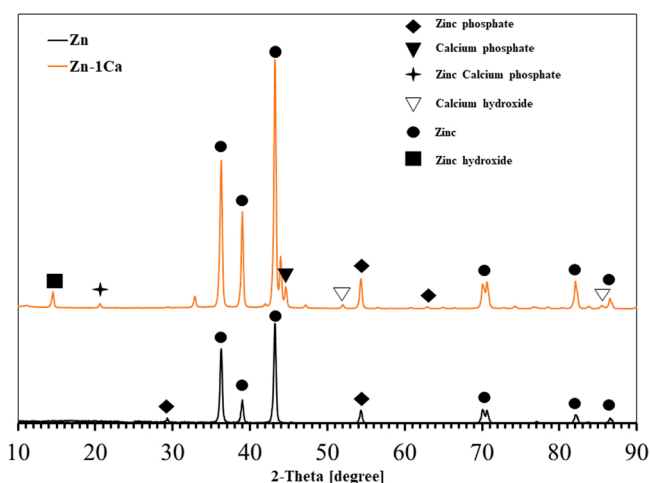**Fig. 18.** XRD analysis of Zn and Zn-1Ca surfaces after anodic polarisation by + 1.5 V vs SCE from OCP in pH 7 0.17 M NaCl containing 1×10^{-3} mol dm^{-3} sodium phosphate.

Zn-1Ca showed the presence of additional Zn hydroxide, Ca phosphate, Ca hydroxide and Zn-Ca phosphate.

4. Discussion

4.1. The corrosion of Zn and Zn-1Ca alloys in pH 7 0.17 M NaCl

Under aerated conditions and at pH 7 Zn corrodes via anodic dissolution of Zn as shown in Eq. (4) and is balanced by cathodic oxygen reduction (Eq. (5)).

$$Zn \rightarrow Zn^{2+} + 2e^- \qquad (4)$$

$$1/2O_2 + H_2O + 2e^- \rightarrow 2OH^- \qquad (5)$$

The cathodic reaction enables the pH in the surface electrolyte to rise above the cathode whilst hydrolysis of the Zn^{2+} causes the pH at the anode to drop. Zn(OH$_2$) will precipitate on the surface once its solubility product (K$_{sp}$ = 1.2×10^{-17} mol^3 dm^{-9}) is exceeded and our characterisation of corrosion products on Zn has confirmed the presence of Zn and O. This relatively low solubility product means that precipitation of Zn (OH)$_2$ tends to limit the pH rise in the surface electrolyte with Zn(OH)$_2$ having a pK$_{a1}$ = 8.96.

In 0.17 M NaCl, localised corrosion can readily occur on Zn as previously observed [40] due to ohmic and pH effects in the solution that

serves to enable localisation. The Zn used in this investigation was galvanising spelter and thus contained small additions of Al to prevent the growth of Zn-Fe intermetallic phases in coated products and is saturated with Fe due to the steel strip passing through the galvanising bath. The formation of Fe_2Al_5 within the alloy could potentially act as initiation points for localised corrosion due to the cathodic nature of this phase. However, Fe_2Al_5 has not been detected in our characterisation of this material so it cannot be conclusively stated that the localisation of corrosion has resulted from galvanic effects. Fe_2Al_5 will often be entrained as dross on top of a solidifying casting and thus it was not observed in the structure of the material used in the experiments.

The data in this investigation have suggested that Zn-1Ca provides superior corrosion performance compared to Zn. Here, it is proposed that this enhanced protection afforded by Zn-1Ca was due to the change in microstructure as Ca addition led to the formation of Zn-Ca intermetallics ($CaZn_{13}$). Once in contact with the electrolyte, this intermetallic phase provides galvanic protection to the Zn phases by preferential anodic dissolution with the release of Ca^{2+} and Zn^{2+} ions. This galvanic protection arises due to the more negative standard reduction potential for Ca of -2.84 V vs SHE compared with -0.76 V vs SHE for Zn. This galvanic activity was supported by the reduction in OCP for the Zn-1Ca compared to Zn after the initial 6 h of stabilisation. The reduction in potential was small due to the alloy composition being 98.5 wt.% Zn but such a difference will cause a preferential galvanic attack at the more active Zn-Ca intermetallic phase. The Ca^{2+} ions released from the intermetallic phase may react with hydroxyl ions (OH^-) generated at the cathode from oxygen reduction to form sparingly soluble Calcium hydroxide ($Ca(OH)_2$, $K_{sp} = 6.5 \times 10^{-6}$ mol^3 dm^{-9}) with a large bandgap of 3.67 eV [41,42]. However, due to the relatively high solubility of $Ca(OH)_2$ the electrolyte above the alloy surface will become enriched with Ca^{2+} and OH^- ions. $Ca(OH)_2$ is a strong base [43,44] that has a pK_{a1} of 12.63 and it has been shown that a saturated solution can develop a pH of 12.5 [45]. Therefore, as anodic release of Ca^{2+} continues the subsequent concentration of OH^- ions in solution from the cathode increases due to the relatively high solubility of $Ca(OH)_2$ enabling the pH of the electrolyte above the alloy surface to rise. A pH of 12.5 may not be reached however due to the competing hydrolysis of Zn^{2+} ions, which will also be released from the intermetallic, to form Zn $(OH)_2$ ($pK_{a1} = 8.96$) and H^+ that will tend to acidify the electrolyte. However, assessing the significantly increased precipitation of corrosion products for the Zn-1Ca alloy compared with Zn in the TLM experiments in Figs. 7 and 8 would suggest that alkalisation has indeed increased. This alkalisation of local pH creates a suitable environment for stabilisation of the pre-existing air-formed Zinc oxide/hydroxides and those forming due to the release of Zn^{2+} from the intermetallic phase, consequently passivating the Zn surface [46]. $Zn(OH)_2$ has a solubility product that is many orders of magnitude less than that of $Ca(OH)_2$ and thus will become the dominant precipitated corrosion product as the alkalisation increases. Thus, in this alloy, the formation of corrosion products is more favoured due to the Ca^{2+} influencing the electrolyte pH above the alloy surface especially over the cathode where the local flux of OH^- ions will be greatest. The cathodic kinetics are subsequently reduced for the Zn-1Ca alloy as demonstrated in the cathodic polarisation curves. The reduction in overall corrosion kinetics for the Zn-1Ca alloy thus seem to be a result of cathodic deactivation due to increased corrosion product precipitation over the cathode enabled by the initial galvanic release of Ca^{2+} ions that serves to increase the surface electrolyte pH thus promoting increased precipitation of zinc hydroxide.

4.2. Inhibition effects of phosphate during corrosion of Zn and Zn-1Ca alloys

4.2.1. The inhibition of Zn corrosion in 0.17 M NaCl containing 1×10^{-3} mol dm^{-3} Na$_3$PO$_4$

For Zn, precipitation of a solid was observed over the anodic site with its thickness seemingly tapering away with distance from the anode in

contrast to corrosion observed on Zn with no phosphate present in solution where the region around the anode remained free from the precipitate. At the anode, the local concentration of Zn^{2+} cations will increase as corrosion is established. These cations subsequently react with the phosphate ions (PO_4^{3-}) present within the electrolyte to precipitate as zinc phosphate ($Zn_3(PO_4)_2$) once the solubility product ($K_{sp} = 9 \times 10^{-33}$ mol^5 dm^{-15}) in the electrolyte is exceeded. The concentration of metal ions is highest immediate to the anode and decreases with distance away from the anode due to cation diffusion and migration. Hence, at the anode sufficient metal ions (Zn^{2+}) become available with time to exceed the solubility limit and precipitation of zinc phosphate is observed local to the anodic site [19] with the extent of precipitation decreasing with distance from the anode. This precipitation serves to passivate the anode, consequently reducing the corrosion activity and thus increasing the corrosion resistance. The K_{sp} for $Zn_3(PO_4)_2$ is many orders of magnitude lower than $Zn(OH)_2$ ($K_{sp} = 1.2 \times 10^{-17}$ mol^3 dm^{-9}) that was the dominant precipitating product in the control Zn experiment and hence precipitation of $Zn_3(PO_4)_2$ serves to reduce the corrosion rate by a significant amount.

This phenomenon of anodic inhibition on the Zn surface by precipitation of a solid phosphate product is supported by the visual precipitation observed in TLM, the reduction in total SVET measured mass loss and hourly mass loss kinetics, the increase in LPR, the positive shift in OCP for the first 8 h indicative of a precipitate forming and the anodic polarisation curves where E_{corr} is shifted to a more positive potential with a subsequent reduction in anodic current compared to the control Zn (Fig. 17).

4.2.2. The inhibition of Zn-1Ca corrosion in 0.17 M NaCl containing 1×10^{-3} mol dm^{-3} Na$_3$PO$_4$

In the case of Zn-1Ca, the $CaZn_{13}$ intermetallic corroded preferentially, evidenced by the darkening of this phase in the TLM experiments and prior to and after immersion EDS of $CaZn_{13}$, protecting the Zn phase, releasing Ca^{2+} and Zn^{2+} into the electrolyte. Ca^{2+} and Zn^{2+} can both react with phosphate ions present within the electrolyte to precipitate protective film(s) containing metal phosphates of Zn, Ca and/or both. The preferential corrosion of $CaZn_{13}$ and its uniform distribution within the microstructure enables a precipitate to form evenly across the sample surface rather than in the more focussed precipitation for the Zn sample where precipitation tended to occur at localised points in the microstructure where an anode had initiated. This enhanced surface coverage may explain the increased inhibition efficiency demonstrated with this system in both the anodic and cathodic polarisation curves when compared to the Zn system indicative of a mixed inhibitor response with a net anodic inhibition effect. Additionally, the more positive potential shift and the longer duration of this shift in OCP further support the notion of enhanced precipitation over the surface with net anodic inhibition.

The alkalisation mechanism due to the presence of Ca^{2+} and OH^- in solution proposed in Section 4.1 could explain the enhanced inhibition performance of phosphate with this alloy. The form of phosphate that exists in solution is dependent on pH through the dissociation of phosphoric acid such that $H_3PO_4 \leftrightharpoons H_2PO_4^- + H^+$ [$pK_{a1} = 2.14$], $H_2PO_4^- \leftrightharpoons HPO_4^{2-} + H^+$ [$pK_{a2} = 7.2$] and $HPO_4^{2-} \leftrightharpoons PO_4^{3-} + H^+$ [$pK_{a3} = 12.4$]. As such, given these equilibria and pKa values, any chemical effect that serves to increase the pH in the electrolyte will increase the proportion of triphosphate ions (PO_4^{3-}) in the electrolyte. The reaction of triphosphates with both Ca^{2+} and Zn^{2+} cations produces insoluble precipitates and thus the increase in pH created by Ca additions serves to facilitate the precipitation of insoluble phosphates thus enhancing the inhibition efficiency. As this is happening uniformly across the surface associated with the $CaZn_{13}$ it becomes further apparent why a better protective film may form. The chemical nature of the precipitate is intriguing. The XRD data determined the presence of zinc hydroxide, zinc phosphate, calcium phosphate, calcium hydroxide and a mixed zinc calcium phosphate. The corrosion data for the Zn alloy has shown that

$Zn_3(PO_4)_2$ will provide anodic inhibition on Zn. The additional reduction in cathodic current observed for Zn-1Ca + Phosphate could be due to the presence of calcium phosphate ($Ca_3(PO_4)_2$ $K_{sp} = 2.07 \times 10^{-33}$ mol^5 dm^{-15}), which has been shown to act as a cathodic inhibitor through the reaction $2HPO_4^{2-} + 2OH^- + 3\ Ca^{2+} = Ca_3(PO_4)_2 + 2H_2O$ [47] and/or due to calcium hydroxide formation at cathodic sites. It has also been found that in the phosphating pre-treatment of metals a modification of zinc phosphate baths with Ca^{2+} ions led to the formation of a more compact structure $Zn_2Ca(PO_4)_2.2H_2O$ with improved corrosion prevention ability [2,18,48,49].

For both Zn and Zn-1Ca with phosphate, the extent of corrosion inhibition seemed to reduce with respect to time in this 0.17 M NaCl electrolyte and in fact, in 48-h SVET experiments, the mass loss measured for both alloys with phosphate over the 2nd 24-h period was similar to that measured for the respective alloys over 24 h just in 0.17 M NaCl. The OCP curves suggest that the precipitates that form may begin to break down as their potentials drop towards those of Zn after 8 h and 12 h respectively for Zn and Zn-1Ca. However, it is demonstrable by this increased time to breakdown and the significantly reduced mass loss kinetics shown in the hourly SVET data that the precipitate formed in the Zn-1Ca seemed to afford better protection over Zn for a longer period.

5. Conclusions

An investigation into the effect of 1 wt% addition of Calcium to Zn on its corrosion mechanism and performance in 0.17 M NaCl has shown that;

- the alloying of Zn with 1 wt% Ca resulted in the formation of discrete, uniformly dispersed intermetallic $CaZn_{13}$ phases throughout the microstructure.
- The 24-h SVET-derived metal loss decreased significantly with 1 wt % Ca additions to Zn. A 56 % decrease in the metal loss was measured for Zn-1Ca compared to the control Zn.
- TLM and EDS analysis revealed that for Zn-1Ca, the corrosion initiated and preferentially attacked the intermetallic $CaZn_{13}$ before progressing into the majority bulk Zn phase. This phase was preferentially galvanically corroded due to the more negative standard reduction potential of Ca highlighted by a decrease in OCP for Zn-1Ca.
- TLM demonstrated that the precipitation of corrosion products was greater for Zn-1Ca and occurred over the cathode.
- LPR showed a decrease in the corrosion rate for Zn-1Ca of 2.5 times and this was supported by a decreased cathodic current during cathodic polarisation for Zn-1Ca.
- The increased precipitation of corrosion products at the cathode resulted in cathodic deactivation and a reduced corrosion rate.

The effect of the addition of 1×10^{-3} mol dm^{-3} Na_3PO_4 to 0.17 M NaCl on the corrosion resistance and mechanisms of Zn and Zn-1Ca alloys has shown that;.

- 24-h SVET-derived metal loss decreased by 48 % for Zn but in presence of Calcium (i.e., Zn-1Ca) a 72 % decrease in metal loss was measured.
- TLM and potentiodynamic polarisation measurements showed that Na_3PO_4 acts as an anodic inhibitor on Zn. EDS and XRD revealed localised precipitation of $Zn_3(PO_4)_2$ corrosion products in the vicinity of focal anodic sites that shifted E_{corr} to more positive potentials with a reduction in anodic current with respect to the control Zn.
- For Zn-1Ca, TLM, OCP and polarisation measurements showed Na_3PO_4 also acts as a net anodic inhibitor but also demonstrated cathodic inhibition.

- TLM revealed the formation of a protective precipitate covering most of the surface of Zn-1Ca. EDS and XRD analysis of the precipitate showed the presence of zinc phosphate, calcium phosphate, calcium hydroxide and a mixed zinc calcium phosphate.
- The increased pH enabled by Ca^{2+} released from uniformly distributed $CaZn_{13}$ phases resulted in increased precipitation of insoluble metal phosphate films leading to both cathodic and anodic deactivation of the alloy.
- It has been demonstrated that by visually observing corrosion mechanisms at a microstructural level in combination with electrochemical techniques, alloy systems may be designed to provide tailored ion release and chemical conditions that may enhance the performance of typical inhibitor systems that are incorporated in organic coatings.

Credit authorship contribution statement

A.D. Malla: Investigation, Methodology, Data curation, Formal analysis, Writing – original draft, Writing – review & editing. **J.H. Sullivan:** Conceptualization, Methodology, Validation, Formal analysis, Supervision, Writing – original draft, Writing – review & editing. **D. Penney:** Conceptualization, Methodology, Validation, Writing – review & editing, Formal analysis, Supervision. **T. Dunlop:** Investigation. **P. Barker:** Supervision, Writing – review & editing.

Declaration of Competing Interest

The authors declare that they have no known competing financial interests or personal relationships that could have appeared to influence the work reported in this paper.

Data Availability

The authors do not have permission to share data.

Acknowledgements

References

[1] I.M. Zin, V.I. Pokhmurskii, J.D. Scantlebury, S.B. Lyon, Model electrochemical cell study of cut-edge corrosion inhibition on coil-coated steel sheet by chromate-, phosphate-, and calcium-containing pigments, J. Electrochem. Soc. 148 (2001) B293, https://doi.org/10.1149/1.1381072.

[2] I.M. Zin, S.B. Lyon, V.I. Pokhmurskii, M.C. Simmonds, Inhibition of steel and galvanised steel corrosion by zinc and calcium ions in the presence of phosphate, Corros. Eng. Sci. Technol. 39 (2004) 167–173, https://doi.org/10.1179/147842204225016967.

[3] A. Dan, P.K. Bijalwan, A.S. Pathak, A.N. Bhagat, A review on physical vapor deposition-based metallic coatings on steel as an alternative to conventional galvanized coatings, J. Coat. Technol. Res. 19 (2022) 403–438, https://doi.org/10.1007/s11998-021-00564-z.

[4] J. Sullivan, N. Cooze, C. Gallagher, T. Lewis, T. Prosek, D. Thierry, In situ monitoring of corrosion mechanisms and phosphate inhibitor surface deposition during corrosion of zinc–magnesium–aluminium (ZMA) alloys using novel time-lapse microscopy, Faraday Discuss. 180 (2015) 361–379, https://doi.org/10.1039/C4FD00251B.

[5] J. Sullivan, S. Mehraban, J. Elvins, In situ monitoring of the microstructural corrosion mechanisms of zinc–magnesium–aluminium alloys using time lapse microscopy, Corros. Sci. 53 (2011) 2208–2215, https://doi.org/10.1016/j.corsci.2011.02.043.

[6] J. Duchoslav, M. Arndt, R. Steinberger, T. Keppert, G. Luckeneder, K. H. Stellnberger, J. Hagler, C.K. Riener, G. Angeli, D. Stifter, Nanoscopic view on the initial stages of corrosion of hot dip galvanized Zn–Mg–Al coatings, Corros. Sci. 83 (2014) 327–334, https://doi.org/10.1016/j.corsci.2014.02.027.

[7] J. Duchoslav, M. Arndt, T. Keppert, G. Luckeneder, D. Stifter, XPS investigation on the surface chemistry of corrosion products on ZnMgAl-coated steel, Anal. Bioanal. Chem. 405 (2013) 7133–7144, https://doi.org/10.1007/s00216-013-7099-3.

[8] T. Prosek, A. Nazarov, U. Bexell, D. Thierry, J. Serak, Corrosion mechanism of model zinc-magnesium alloys in atmospheric conditions, Corros. Sci. 50 (2008) 2216–2231, https://doi.org/10.1016/j.corsci.2008.06.008.

[9] P. Volovitch, C. Allely, K. Ogle, Understanding corrosion via corrosion product characterization: I. Case study of the role of Mg alloying in Zn–Mg coating on steel, Corros. Sci. 51 (2009) 1251–1262, https://doi.org/10.1016/j.corsci.2009.03.005.

[10] S. Schuerz, M. Fleischanderl, G.H. Luckeneder, K. Preis, T. Haunschmied, G. Mori, A.C. Kneissl, Corrosion behaviour of Zn – Al – Mg coated steel sheet in sodium chloride-containing environment, Corros. Sci. 51 (2009) 2355–2363, https://doi.org/10.1016/j.corsci.2009.06.019.

[11] S. Schürz, G.H. Luckeneder, M. Fleischanderl, P. Mack, H. Gsaller, A.C. Kneissl, G. Mori, Chemistry of corrosion products on Zn–Al–Mg alloy coated steel, Corros. Sci. 52 (2010) 3271–3279, https://doi.org/10.1016/j.corsci.2010.05.044.

[12] N. Wint, A.D. Malla, N. Cooze, T. Savill, S. Mehraban, T. Dunlop, J.H. Sullivan, D. Penney, G. Williams, H.N. McMurray, The ability of Mg2Ge crystals to behave as 'smart release' inhibitors of the aqueous corrosion of Zn-Al-Mg alloys, Corros. Sci. 179 (2021), 109091, https://doi.org/10.1016/j.corsci.2020.109091.

[13] S.A. Katz, The analytical biochemistry of chromium, Environ. Health Perspect. 92 (1991) 13–16, https://doi.org/10.1289/ehp.919213.

[14] Z. Fang, M. Zhao, H. Zhen, L. Chen, P. Shi, Z. Huang, Genotoxicity of Tri- and hexavalent chromium compounds in vivo and their modes of action on DNA damage in vitro, PLoS One 9 (2014), e103194, https://doi.org/10.1371/journal.pone.0103194.

[15] R.M. Park, J.F. Bena, L.T. Stayner, R.J. Smith, H.J. Gibb, P.S.J. Lees, Hexavalent chromium and lung cancer in the chromate industry: a quantitative risk assessment, Risk Anal. 24 (2004) 1099–1108, https://doi.org/10.1111/j.0272-4332.2004.00512.x.

[16] H.J. Gibb, P.S.J. Lees, P.F. Pinsky, B.C. Rooney, Lung cancer among workers in chromium chemical production, Am. J. Ind. Med. 38 (2000) 115–126, https://doi.org/10.1002/1097-0274(200008)38:2<115::AID-AJIM1>3.0.CO;2-Y.

[17] P. Zarras, J.D. Stenger-Smith, Smart inorganic and organic pretreatment coatings for the inhibition of corrosion in metals/alloys, Intell. Coat. Corros. Control (2015), https://doi.org/10.1016/B978-0-12-411467-8.00003-9.

[18] A.A. al-Swaidani, Modified zinc phosphate coatings: a promising approach to enhance the anti-corrosion properties of reinforcing steel, MOJ Civ. Eng. 3 (2017), https://doi.org/10.15406/mojce.2017.03.00083.

[19] J. Sullivan, N. Cooze, C. Gallagher, T. Lewis, T. Prosek, D. Thierry, In situ monitoring of corrosion mechanisms and phosphate inhibitor surface deposition during corrosion of zinc-magnesium-aluminium (ZMA) alloys using novel time-lapse microscopy, Faraday Discuss. 180 (2015) 361–379, https://doi.org/10.1039/c4fd00251b.

[20] S.M. Powell, H.N. McMurray, D.A. Worsley, Use of the scanning reference electrode technique for the evaluation of environmentally friendly, nonchromate corrosion inhibitors, CORROSION 55 (1999) 1040–1051, https://doi.org/10.5006/1.3283941.

[21] K. Aramaki, The inhibition effects of chromate-free, anion inhibitors on corrosion of zinc in aerated 0.5 M NaCl, Corros. Sci. 43 (2001) 591–604, https://doi.org/10.1016/S0010-938X(00)00085-8.

[22] H.H. Uhlig, D.N. Triadis, M. Stern, Effect of oxygen, chlorides, and calcium ion on corrosion inhibition of iron by polyphosphates, J. Electrochem. Soc. 102 (1955) 59, https://doi.org/10.1149/1.2429995.

[23] Z. Szklarska-Smialowska, J. Mańkowski, Cathodic inhibition of the corrosion of mild steel in phosphate, tungstate, arsenate and silicate solutions containing Ca^{2+} ions, Br. Corros. J. 4 (1969) 271–275, https://doi.org/10.1179/bcj.1969.4.5.271.

[24] J. Sullivan, N. Cooze, C. Gallagher, T. Lewis, T. Prosek, D. Thierry, In situ monitoring of corrosion mechanisms and phosphate inhibitor surface deposition during corrosion of zinc-magnesium-aluminium (ZMA) alloys using novel time-lapse microscopy, Faraday Discuss. (2015), https://doi.org/10.1039/c4fd00251b.

[25] N. Wint, N. Cooze, J.R. Searle, J.H. Sullivan, G. Williams, H.N. McMurray, G. Luckeneder, C. Riener, The effect of microstructural refinement on the localized corrosion of model Zn-Al-Mg alloy coatings on steel, J. Electrochem. Soc. 166 (2019) C3147–C3158, https://doi.org/10.1149/2.0171911jes.

[26] J. Elvins, J.A. Spittle, D.A. Worsley, Microstructural changes in zinc aluminium alloy galvanising as a function of processing parameters and their influence on corrosion, Corros. Sci. 47 (2005) 2740–2759, https://doi.org/10.1016/j.corsci.2004.11.011.

[27] J. Elvins, J.A. Spittle, J.H. Sullivan, D.A. Worsley, The effect of magnesium additions on the microstructure and cut edge corrosion resistance of zinc aluminium alloy galvanised steel, Corros. Sci. 50 (2008) 1650–1658, https://doi.org/10.1016/j.corsci.2008.02.005.

[28] D.J. Penney, J.H. Sullivan, D.A. Worsley, Investigation into the effects of metallic coating thickness on the corrosion properties of Zn-Al alloy galvanising coatings, Corros. Sci. 49 (2007) 1321–1339, https://doi.org/10.1016/j.corsci.2006.07.006.

[29] D.A. Worsley, H.N. McMurray, J.H. Sullivan, I.P. Williams, Quantitative assessment of localized corrosion occurring on galvanized steel samples using the scanning vibrating electrode technique, Corrosion 60 (2004) 437–447, https://doi.org/10.5006/1.3299239.

[30] A.C. Bastos, M.L. Zheludkevich, M.G.S. Ferreira, Concerning the efficiency of corrosion inhibitors as given by SVET, Port. Electrochim. Acta (2008), https://doi.org/10.4152/pea.200801047.

[31] G. Williams, H.Neil McMurray, Localized corrosion of magnesium in chloride-containing electrolyte studied by a scanning vibrating electrode technique, J. Electrochem. Soc. 155 (2008) C340, https://doi.org/10.1149/1.2918900.

[32] G. Williams, H.N. McMurray, Pitting corrosion of steam turbine blading steels: the influence of chromium content, temperature, and chloride ion concentration, Corrosion (2006), https://doi.org/10.5006/1.3278269.

[33] J. Sullivan, C. Weirman, J. Kennedy, D. Penney, Influence of steel gauge on the microstructure and corrosion performance of zinc alloy coated steels, Corros. Sci. 52 (2010) 1853–1862, https://doi.org/10.1016/j.corsci.2010.02.032.

[34] H. Okamoto, Ca-Zn (calcium-zinc), J. Phase Equilibr. Diffus 34 (2013) https://doi.org/10.1007/s11669-012-0180-3 (171–171).

[35] H.F. Li, X.H. Xie, Y.F. Zheng, Y. Cong, F.Y. Zhou, K.J. Qiu, X. Wang, S.H. Chen, L. Huang, L. Tian, L. Qin, Development of biodegradable Zn-1X binary alloys with nutrient alloying elements Mg, Ca and Sr, Sci. Rep. 5 (2015) 10719, https://doi.org/10.1038/srep10719.

[36] H. Li, H. Yang, Y. Zheng, F. Zhou, K. Qiu, X. Wang, Design and characterizations of novel biodegradable ternary Zn-based alloys with IIA nutrient alloying elements Mg, Ca and Sr, Mater. Des. 83 (2015) 95–102, https://doi.org/10.1016/j.matdes.2015.05.089.

[37] Y. Zou, X. Chen, B. Chen, Effects of Ca concentration on degradation behavior of Zn-x Ca alloys in Hank's solution, Mater. Lett. (2018), https://doi.org/10.1016/j.matlet.2018.02.018.

[38] N. Yang, N. Balasubramani, J. Venezuela, S. Almathami, C. Wen, M. Dargusch, The influence of Ca and Cu additions on the microstructure, mechanical and degradation properties of Zn–Ca–Cu alloys for absorbable wound closure device applications, Bioact. Mater. (2021), https://doi.org/10.1016/j.bioactmat.2020.10.015.

[39] T. Lewis, Investigation into the Corrosion Behaviour and Effect of Inhibitor Additions on Commercial Zn-Mg-Al Alloys, Swansea University, 2018.

[40] N. Wint, K. Khan, J.H. Sullivan, H.N. McMurray, Concentration effects on the spatial interaction of corrosion pits occurring on zinc in dilute aqueous sodium chloride, J. Electrochem. Soc. 166 (2019) 3028–3038, https://doi.org/10.1149/2.0051911jes.

[41] Y. Aierken, H. Sahin, F. Iyikanat, S. Horzum, A. Suslu, B. Chen, R.T. Senger, S. Tongay, F.M. Peeters, Portlandite crystal: bulk, bilayer, and monolayer structures, Phys. Rev. B 91 (2015), 245413, https://doi.org/10.1103/PhysRevB.91.245413.

[42] C. Xia, W. Xiong, J. Du, T. Wang, Z. Wei, J. Li, Robust electronic and mechanical properties to layer number in 2D wide-gap $X(OH)_2$ (X = Mg, Ca), J. Phys. D Appl. Phys. 51 (2018), 015107, https://doi.org/10.1088/1361-6463/aa996e.

[43] A. Farhad, Z. Mohammadi, Calcium hydroxide: a review, Int. Dent. J. 55 (2005) 293–301, https://doi.org/10.1111/j.1875-595X.2005.tb00426.x.

[44] L.R.G. Fava, W.P. Saunders, Calcium hydroxide pastes: classification and clinical indications, Int. Endod. J. 32 (1999) 257–282, https://doi.org/10.1046/j.1365-2591.1999.00232.x.

[45] R.G. Bates, V.E. Bower, E.R. Smith, Calcium hydroxide as a highly alkaline pH standard, J. Res. Natl. Bur. Stand 56 (1956) (1934) 305, https://doi.org/10.6028/jres.056.040.

[46] S. Thomas, I.S. Cole, M. Sridhar, N. Birbilis, Revisiting zinc passivation in alkaline solutions, Electrochim. Acta 97 (2013) 192–201, https://doi.org/10.1016/j.electacta.2013.03.008.

[47] V.I. Pokhmurs'kyi, I.M. Zin, S.B. Layon, L.M. Bilyi, Synergistic effect of phosphate and calcium-containing pigments on the corrosion resistance of galvanized steel, Mater. Sci. (2003), https://doi.org/10.1023/B:MASC.0000010264.27310.9e.

[48] R. Zeng, Z. Lan, L. Kong, Y. Huang, H. Cui, Characterization of calcium-modified zinc phosphate conversion coatings and their influences on corrosion resistance of AZ31 alloy, Surf. Coat. Technol. 205 (2011) 3347–3355, https://doi.org/10.1016/j.surfcoat.2010.11.027.

[49] I.M. Zin, S.B. Lyon, V.I. Pokhmurskii, Corrosion control of galvanized steel using a phosphate/calcium ion inhibitor mixture, Corros. Sci. 45 (2003) 777–788, https://doi.org/10.1016/S0010-938X(02)00130-0.